

Structural and thermal evolution of an infant subduction shear zone: Insights from sub-ophiolite metamorphic rocks recovered from Oman Drilling Project Site BT-1B

Alissa J. Kotowski^{1*}, Mark Cloos¹, Daniel F. Stockli¹, Eytan Bos Orent^{1†}

¹Department of Geological Sciences, Jackson School of Geosciences, University of Texas at Austin, USA

Key Points:

- The low-temperature metamorphic sole beneath the Samail Ophiolite records subduction and return flow before juxtaposition with the ophiolite
- High sample density of the 104 m-thick core reveals it comprises 3 lithologically distinct subunits that record a weak inverted P-T gradient
- Low-T sole rocks reached similar peak P as the high-T sole but colder peak T (8-12 kbar, 500°C) and witnessed rapid interface refrigeration

*now at Department of Earth and Planetary Sciences, McGill University

†now at Department of Geosciences, University of Arizona

Corresponding author: Alissa J. Kotowski, alissa.kotowski@mcgill.ca

Abstract

The thermal structure of the subduction interface changes drastically within the first few million years following subduction initiation (i.e. *subduction infancy*), resulting in changing metamorphic conditions and degree of mechanical coupling. Metamorphic soles beneath ophiolites record snapshots of subduction infancy. Beneath the Samail Ophiolite (Oman), the sole comprises structurally higher high-temperature (HT) and lower low-temperature (LT) units. This apparent inverted metamorphic gradient has been attributed to metamorphism under different Pressure-Temperature (P-T) conditions along the interface. However, peak P-T and timing of LT sole subduction are poorly constrained. Samples from Oman Drilling Project core BT-1B (104 m of metamorphic rocks) reveal that the LT sole subducted to similar peak P as the HT sole, but experienced $\sim 300^\circ\text{C}$ lower peak T. Prograde fabrics in meta-sedimentary and meta-mafic rocks record Si-in-phengite values and amphibole chemistries consistent with peak P-T of $\sim 8\text{--}12$ kbar and $\sim 450\text{--}550^\circ\text{C}$ in the epidote-amphibolite facies. Retrograde fabrics record a transition from near pervasive ductile to localized brittle strain under greenschist facies conditions. Titanite U-Pb ages (two samples) constrain timing of peak LT sole subduction to 95.7 ± 1.1 Ma, which may post-date the HT sole by $\sim 6\text{--}8$ Myr. In light of previous HT sole thermobarometry and geochronology, these new results support a model of protracted subduction and accretion while the infant subduction zone cooled at rates of $\sim 100^\circ\text{C}/\text{Myr}$ for $\sim 1\text{--}5$ Myr. Temporal overlap of LT sole metamorphism and ophiolite crust formation suggests that underthrusting and cooling may lead to interface weakening, facilitating upper plate extension and forearc spreading.

1 Introduction

When subduction initiates at speeds of several cm/yr, the first few million years of convergence (i.e., '*subduction infancy*') involve high-temperature metamorphism of underthrust material, cooling of the hanging wall block, and underplating with downward strain localization along the new plate boundary (e.g. Stern & Bloomer, 1992). The nature of interplate coupling evolves as the metamorphic assemblages and rock types, thermal structure, and rock rheologies change (Ruh et al., 2015; Agard et al., 2016; Soret et al., 2017). Numerical models demonstrate that interface weakening and progressive strain localization control the depths where materials are underplated along the shallow interface (Ruh et al., 2015) as well as large-scale, induced convection in the asthenosphere (e.g., Gurnis et al.,

2004; Wada et al., 2008; Wada & Wang, 2009; Coltice et al., 2017). Quantifying prograde and retrograde Pressure-Temperature (P-T) trajectories recorded by metamorphic rocks that form during subduction infancy provides insight into how interplate coupling varies with depth and through time. These constraints lead to a refined understanding of geodynamic feedbacks between interface cooling rates, presence/absence of fluids, and operative deformation mechanisms, which conspire to either promote or suppress subduction following initial convergence (cf. Agard et al., 2020).

Tectonometamorphic evidence for interface behavior during subduction infancy is preserved in the geologic record as thin (~ 10 -500 m) zones of metamorphosed oceanic crust and sedimentary rocks beneath ophiolites, called *metamorphic soles* (Williams & Smyth, 1973; Dewey, 1976; Wakabayashi & Dilek, 2000). In Newfoundland (Williams & Smyth, 1973; Dewey & Casey, 2013), Turkey (Çelik et al., 2011; Wakabayashi & Dilek, 2000), and Oman (Ghent & Stout, 1981; Hacker & Gnos, 1997) (Fig. 1), large-slab ophiolites have extensive exposures of metamorphic soles that record hot temperature-depth trajectories for ~ 5 -10 Myr after subduction initiation. These soles consist of a thin (\sim m to 10's of m) structurally higher, garnet-amphibolite to granulite facies high-temperature section ('HT sole') and a thicker (~ 10 's to several 100's m) structurally lower, greenschist facies low-temperature section ('LT sole') (Fig. 1B). The apparent inverted metamorphic gradient was originally attributed to downwards conductive heating from a hot mantle wedge, sometimes described as the 'ironing effect' (e.g., Jamieson, 1981; Gnos & Peters, 1992; Hacker & Mosenfelder, 1996). More recently, several researchers have argued that HT and LT sections are distinct tectonic units that were metamorphosed under different P-T conditions and were progressively accreted before ophiolite emplacement (Searle & Cox, 1999; Agard et al., 2016, 2020; Soret et al., 2017).

Beneath the Samail Ophiolite in Oman, metamorphic sole rocks crop out as discontinuous lenses along its entire ~ 550 km length (Fig. 1). Structural, petrologic, and geochronologic investigations at various locations have resolved a history of subduction and underplating starting at ~ 94 -95 Ma and potentially as early as ~ 104 Ma, as recorded by garnet-bearing HT rocks (e.g., Searle & Malpas, 1980; Searle & Cox, 1999; Hacker, 1994; Hacker et al., 1996; Cowan et al., 2014; Soret et al., 2017; Guilmette et al., 2018). However, the timing of deformation and conditions of metamorphism in the structurally thicker, finer grained, garnet-absent LT part of the sole is much less studied (Bucher, 1991; Hacker et al., 1996; Gnos, 1998). Specifically, it remains unclear whether the HT and LT soles experienced

different P-T conditions at the same time, or the LT sole was diachronously subducted and accreted after the HT sole. If the latter is true, then LT metamorphic soles may contain valuable, yet thus far underappreciated, petrologic and geochronologic information that can constrain the thermal and rheological evolution of subduction shear zones during infancy.

In this study, we present new structural, petrologic, and geochronologic data that refine the deformation and metamorphism history of LT sole rocks that were sampled at Oman Drilling Project site BT-1B (Fig. 1). In this core, a 40 cm-thick cataclastic fault zone separates 195 m of hydrated (serpentinite) and carbonated (listvenite) ultramafic rocks from a 104 m thick section of LT sole. We present data from a densely sampled suite of rocks that span the entire 104 m of core to distinguish prograde from retrograde fabrics, constrain corresponding P-T conditions, and U-Pb date syn-kinematic, prograde and retrograde titanite crystallization. This work reveals new information about the tectonic relationship between the HT and LT sole slivers, and has implications for rates of refrigeration and evolving interface dynamics during subduction infancy.

2 Geologic Context

The Samail Ophiolite, with an outcropping area of $\sim 20,000 \text{ km}^2$, is the most complete and best-exposed subaerial complex of oceanic crust and upper mantle in the world. Spanning $\sim 550 \text{ km}$ N-S and $\sim 100\text{-}150 \text{ km}$ E-W along the coastline of Oman and the United Arab Emirates, the ophiolite comprises $\sim 4\text{-}7 \text{ km}$ of oceanic crustal rocks atop $\sim 8\text{-}12 \text{ km}$ of mantle peridotite (Allemann, 1972; Lippard, 1986; Nicolas et al., 1988) (Fig. 1). Zircon U-Pb ages from plagiogranites from eight locations in upper-level gabbros constrain ophiolite crystallization between $\sim 96.4\text{-}95.5 \text{ Ma}$ along its entire length (Tilton et al., 1981; Rioux et al., 2012, 2013) (Fig. 1A). At the base of the ultramafic portion of the ophiolite, a ductile shear zone and/or fault contact juxtaposes the lithospheric mantle with discontinuous km-scale lenses of metamorphic sole rocks up to $\sim 200 \text{ m}$ thick (Hacker and Mosenfelder (1996), black lenses in Fig. 1A). The ophiolite-sole package rests structurally atop a weakly metamorphosed and variably imbricated section of Arabian continental proximal and distal margin (Searle & Malpas, 1980) (Fig. 1B). The western leading edge of the ophiolite appears to have been transported as much as 250 km during underthrusting of the Arabian continental margin in the Upper Cretaceous (Glennie, 1974). Offsets along individual post-metamorphic out-of-sequence thrusts and normal faults are up to several kilometers, but large portions of the ophiolite have remained remarkably intact (Nicolas et al., 1988).

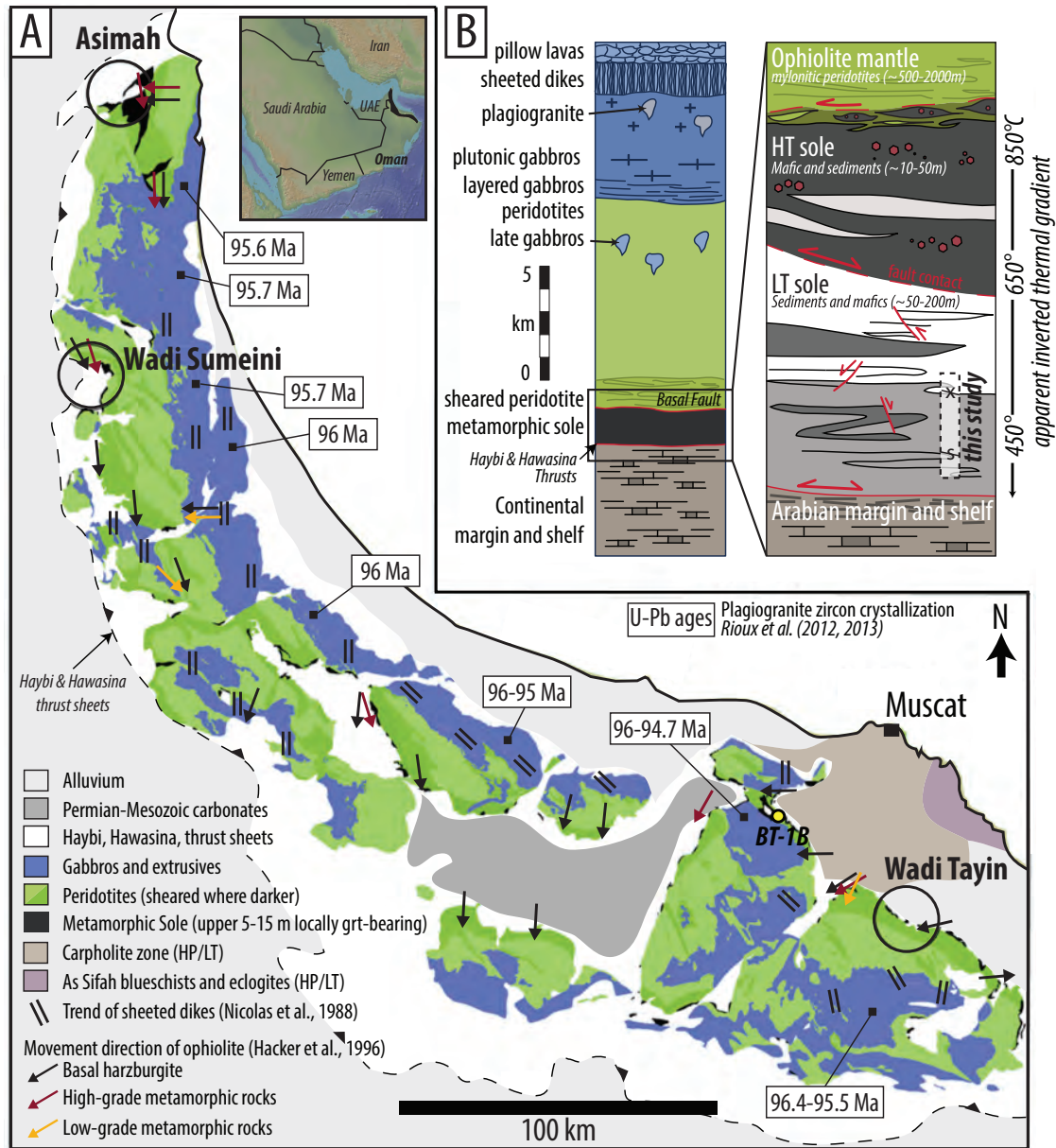


Figure 1: (A) Geologic map of the Samail ophiolite, modified from Agard et al. (2016). OmanDP Site BT-1B is shown in the filled yellow circle. Large black circles correspond to the three best-studied areas where metamorphic sole rocks are exposed. Orientation of sheeted dikes and movement directions (mineral and stretching lineations) compiled by Hacker et al. (1996), after Nicolas et al. (1988). Plagiogranite zircon crystallization ages shown in white boxes are from Rioux et al. (2012, 2013). (B) Schematic ophiolite sequence, modified from Hacker et al. (1996). Inset shows the metamorphic sole. In this idealized sketch, the 100 m of metamorphic rocks in core BT-1B are marked by the dashed grey box labeled 'this study.' The core records a lithologic change (marked by the 'x') and a possible structural discontinuity (marked by 's'). Red double-headed arrows indicate likely reactivation of thrusts as normal faults.

While ophiolites are recognized as slabs of oceanic crust and upper mantle, the geodynamic setting for their formation is much debated. Many workers have long posited that the Samail Ophiolite formed at a mid-ocean spreading ridge (Hopson et al., 1981; Boudier et al., 1985; Hacker, 1991, 1994), on the basis of immobile trace element compositional data from older basalts and gabbros (Godard et al., 2006). In this scenario, emplacement-related thrusting initiated along the ridge axis (Hacker, 1991; Agard et al., 2007, 2014; Duretz et al., 2016). In contrast, a competing model argues that the Samail Ophiolite formed above a subducting plate, in a supra-subduction zone setting (Searle & Malpas, 1980, 1982; Alabaster et al., 1982; Searle & Cox, 2002; MacLeod et al., 2013). This model is supported by younger ophiolitic lavas characterized by up-section decreasing abundances of incompatible elements and increasing LILEs relative to N-MORB (Pearce et al., 1981; Alabaster et al., 1982; Ishikawa et al., 2002). MacLeod et al. (2013) went further using petrologic models of immobile major elements and argued that even the relatively early axial volcanics and dike sequences exhibit fractionation trends that require water concentrations significantly higher than any N-MORB. They concluded that the magmatism was comparable to modern intra-oceanic forearc spreading systems. In the supra-subduction model, the ophiolite formed and then was emplaced atop the Arabian continental margin as the NE-dipping subduction zone was jammed during continental subduction (Searle & Malpas, 1980, 1982; Lippard, 1986; Searle & Cox, 1999).

2.1 Origin and evolution of the metamorphic sole

Structural and geochemical constraints from sub-ophiolite metamorphic rocks provide further insight into the geodynamic processes that led to formation of the Samail Ophiolite. In Oman and the UAE, similar to other global ophiolite exposures, the metamorphic sole is in tectonic contact against variably sheared and partially serpentized basal mantle peridotites. The contact is mostly exposed as a brittle fault zone, although locally the HT sole-mantle contact is a ductile shear zone (e.g. Sumeini and Asimah). The HT unit comprises meters-to-tens of meters-thick garnet-amphibolites and less common garnet-granulites, and locally contains lenses of crystallized partial melt. The HT unit is structurally above a LT unit of tens-to-several hundreds of meters-thick greenschist facies metamorphosed sedimentary rocks and basalts (Bucher, 1991; Searle & Malpas, 1980, 1982; Hacker & Mosenfelder, 1996; Searle & Cox, 2002) (Fig. 1B). Trace element geochemistry of the HT sole suggest the protoliths were both E-MORB and N-MORB that were not genetically related to lavas

in the ophiolite (Searle & Cox, 2002; Ishikawa et al., 2002). This seemingly rules out the simple model of subduction initiation at a mid-oceanic spreading ridge.

Estimates of metamorphic conditions from garnet-pyroxene thermometry, petrologic phase equilibria, and pseudosection phase modeling indicate the HT sole reached ~ 750 - 850°C and 10-14 kbar (Ghent & Stout, 1981; Searle & Malpas, 1982; Gnos, 1998; Hacker & Gnos, 1997; Hacker & Mosenfelder, 1996; Searle & Cox, 2002; Cowan et al., 2014; Soret et al., 2017). Pressure estimates of 10-14 kbar are equivalent to ~ 35 - 50 km depth, and are ~ 2 - 3 x times greater than the ~ 12 - 20 km exposed thickness of the ophiolite section in Oman. This is considered strong evidence that the HT sole rocks were subducted and partially exhumed prior to arriving at their present structural location against the ophiolite (e.g., Hacker & Gnos, 1997; Searle & Cox, 2002; Cowan et al., 2014; Soret et al., 2017). Part of the exhumation was probably accommodated by extensional thinning of the ophiolite by ductile shearing and/or normal faulting which may have removed $\sim 50\%$ of the overburden.

U-Pb zircon crystallization ages from ophiolite plagiogranites and leucocratic lenses in HT sole garnet amphibolites essentially overlap (e.g. 95.3 ± 0.2 Ma (ophiolite) vs. 94.48 ± 0.23 Ma (sole) from Warren et al. (2005); 96.12 - 95.5 Ma (ophiolite) vs. 96.16 ± 0.022 and 94.82 ± 0.035 Ma (sole) from Rioux et al. (2016)). This suggests that formation of oceanic crust and HT metamorphism were concurrent. However, recently published garnet Lu-Hf for three samples from the HT sole (Wadi Tayin and Wadi Sumeini localities, Fig. 1A) yielded ages of ~ 103 - 104 Ma, suggesting that HT sole metamorphism pre-dated igneous crystallization of the ophiolitic crust by ~ 8 Myr (Guilmette et al., 2018). More work is needed to corroborate the reliability of these critical Lu-Hf ages as these garnets appear riddled with inclusions, and zircon micro-inclusions could result in erroneously old ages (cf. Connelly, 2006). If these garnet Lu-Hf ages are correct, then the U-Pb zircon ages from the HT sole date the timing of partial melt crystallization rather than the initial high-temperature subduction-related metamorphism.

While the garnet-bearing HT sole has received lots of attention, the metamorphic and deformational history of the more voluminous LT sole has been largely neglected. In Oman, early studies suggested that the LT sole was a ‘monometamorphic’ unit, freezing in a single greenschist facies event during emplacement beneath the HT unit (Allemann, 1972; Glennie, 1974; Ghent & Stout, 1981). However, observations from Asimah (Bucher, 1991) and from Wadi Sumeini and Wadi Tayin (Hacker & Mosenfelder, 1996), suggested that the

LT sole reached epidote-amphibolite facies prior to a near-pervasive greenschist facies overprint. Amphibole-plagioclase thermobarometry and Raman spectroscopy on carbonaceous material suggested peak P-T of $\sim 4.5\text{--}5.5$ kbar and $\sim 450\text{--}500^\circ\text{C}$ and greenschist facies retrogression at $\sim 340\text{--}380^\circ\text{C}$ (Bucher, 1991; Hacker & Mosenfelder, 1996; Gnos, 1998; Soret et al., 2017). The timing of metamorphism in the LT sole is poorly constrained, but white mica Ar/Ar and biotite K/Ar ages bracket cooling through $\sim 450\text{--}350^\circ\text{C}$ between $\sim 95\text{--}90$ Ma (Gnos & Peters, 1992; Hacker, 1994; Hacker et al., 1996; Guilmette et al., 2018). Other than the garnet Lu-Hf ages, these Ar ages are only 2-3 million years younger than ages reported for the HT sole.

2.2 Recovery of LT sole rocks during the OmanDP and key objectives at Site BT-1B

The Oman Drilling Project (OmanDP) was a multi-national research endeavor motivated to better understand the processes that create and modify oceanic crust and shallow mantle lithosphere. OmanDP sampled key components of the Samail Ophiolite from the crust through the ‘Basal Thrust’ in nine diamond-cored and six rotary-drilled boreholes. In March 2017 at Site BT-1B, on the north side of Wadi Mansah and ~ 50 km NW of Wadi Tayin, 300 m of core was extracted with 100% recovery (Fig. 2). BT-1B comprises 196 m of mantle-derived rocks, the ‘Basal Thrust’ fault zone, and 104 m of sub-ophiolite metamorphic rocks. The depth to the underlying Hawasina continental margin platform sediments and Haybi volcanic rocks is unknown, but probably less than several hundred meters. Herein we refer to the ‘Basal Thrust’ as the ‘Basal Fault,’ since most recent displacement along this structure is likely extensional and associated with post-obduction unroofing and exhumation. Site BT-1B is the only OmanDP core that sampled the Basal Fault and sub-ophiolite metamorphic sole rocks.

Mantle rocks above the Basal Fault at Site BT-1B are a globally rare assemblage of listvenite (carbonated peridotite) containing lenses of serpentinite. The key objective at Site BT-1B was to conduct a detailed study of chemical and structural processes controlling mass transfer along the shallow subduction interface into the overriding mantle wedge, which can absorb carbon in the form of Mg-carbonates (Falk & Kelemen, 2015; Kelemen & Manning, 2015). Characterization of the sub-ophiolite metamorphic sole provides insight into the timing of listvenitization relative to juxtaposition of the sole below the ophiolite and the

potential sources of CO₂-rich fluids linked to low-temperature listvenitization ($\sim 50\text{--}250^\circ\text{C}$; Beinlich et al. (2020)).

On-site core characterization discovered that the sub-ophiolite metamorphics did not contain the HT garnet-bearing sole, instead comprising 104 continuous meters of “low-temperature” (LT) sole. Descriptions of comparable outcrop thicknesses of the LT sole are rarely reported. The ‘most complete’ section of metamorphic sole in Oman crops out ~ 250 km to the NW at Sumeini, and comprises ~ 80 m of HT sole overlying $\sim 20\text{--}30$ m meters of LT sole (Searle & Malpas, 1980; Cowan et al., 2014; Soret et al., 2017). At Asimah, at least $\sim 70\text{--}80$ m of faulted garnet-bearing amphibolite sole is exposed and transitions downward into LT sole rocks composed of epidote + quartz amphibolites and quartzites (Allemann, 1972; Gnos & Peters, 1992; Gnos, 1998; Soret et al., 2017). At Wadi Tayin, the sole consists of ~ 230 m of hornblende-plagioclase amphibolites with only the uppermost ~ 15 m containing garnet (Searle & Malpas, 1980; Ghent & Stout, 1981; Hacker & Mosenfelder, 1996; Soret et al., 2017). The distinction between the HT and LT sole at Wadi Tayin is unclear as the ≥ 100 m thick basal section has been described both as greenschist facies LT sole (Ghent & Stout, 1981) and as an epidote-amphibolite facies sliver with a greenschist facies overprint (Hacker & Mosenfelder, 1996).

3 Lithologic and structural overview

The upper 196 m of core BT-1B comprise variably deformed, locally mylonitic, white and red (iron oxyhydroxide stained) listvenite and several cm’s to ~ 7 m thick horizons of serpentinite (Fig. 2A,B). Intervals of breccia cm’s to 10’s of cm’s thick and cm’s thick cataclasites are abundant, and planar faults are rare (e.g. Fig. 2C; cf. Menzel et al. (2020)). At 196 m, the Basal Fault is characterized by a ~ 40 cm thick zone of fault gouge and ultracataclasite (Fig. 3).

The 104 m section of sub-ophiolite metamorphic rocks can be subdivided into three sections marked by lithological and/or structural boundaries. The upper 34 m (196–230 m) comprise mostly phyllitic, blue-grey to grey-green, metasedimentary rocks (Section 1). Section 1 produces a strong positive excursion in Natural Gamma Ray (NGR) intensity relative to overlying listvenites and underlying meta-mafics, and the bulk density of the listvenites and phyllites are surprisingly similar at ~ 2.7 g/cm³ (Fig. 2A,B). Two collected samples (203 m and 209.1 m) are derived from ~ 30 cm-thick calcite-bearing intervals, described as

calc-phyllites. A lithologic change marks the transition to Section 2, which comprises ~ 60 m (230-290 m) of schistose meta-mafic rocks containing ~ 30 -50% epidote by volume that is visually distinct at the core scale. The transition between Sections 1 and 2 appears sharp in physical properties data (e.g. decrease in NGR and increase in bulk density to ~ 2.9 g/cm³; Fig. 2) but is characterized by a gradual increase of intercalated meta-mafic material between ~ 215 -230 m, until the core becomes entirely meta-mafic at ~ 230 m. Towards the bottom of Section 2 between ~ 275 -290 m, epidote-rich schist alternates on the ~ 10 -50 cm scale with rocks comprising variably deformed, blocky-to-elongated epidote + albite aggregates in a fine-grained amphibole-rich matrix. Lithologic transitions are typically gradational and therefore may represent some relict, primary compositional layering, but are locally marked by discrete fault boundaries. A lithological and/or structural change marks the transition to Section 3, which comprises 10 m (290-300 m) of fine-grained blue-black amphibole-rich schists. The Section 2-3 transition is not as obvious in physical properties data, but may be marked by a small positive excursion in NGR at 290 m (Fig. 2A).

Throughout the 104 m of core, penetrative ductile fabrics are cross-cut by numerous faults with thin cataclastic zones, as well as several zones up to a few tens of cm thick of cataclasis and brecciation (grey dashed lines in Fig. 2). The thickest interval logged as breccia in the core occurs at 244 m and is ~ 40 cm thick. Planar faults and thin cataclastic breccia zones are more abundant in the meta-mafics compared to phyllites (Fig 2C). Offset along the thin cataclastic breccia zones is uncertain, but is probably at least tens of centimeters because some fabric discordance is common on either side of brecciated horizons. The amount of offset across most of the planar faults is unknown, but probably small as few juxtapose discernible changes in lithology. The most obvious change in lithology that implies large (probably meters) displacements is present at 285 m where a layer of epidote + albite aggregate-bearing schist is sharply juxtaposed against a fine-grained epidote-amphibole schist (Fig. 3A, panel 285 m). Notably, planar faults and cataclastic breccias are sparse in the lower 50 m of the carbonated ultramafics.

The dominant foliation is generally near-perpendicular to the core's long axis and thus is dipping shallowly to moderately, given the Hole BT-1B inclination of $\sim 80^\circ$. This is consistent with field observations of the listvenite-sole contact near Site BT-1B (cf. Menzel et al., 2020). Intervals of core up to ~ 70 cm long have a foliation that dips obliquely (up to $\sim 45^\circ$) suggesting that the core may have intersected several meter-scale folds, such as those reported by Soret et al. (2017).

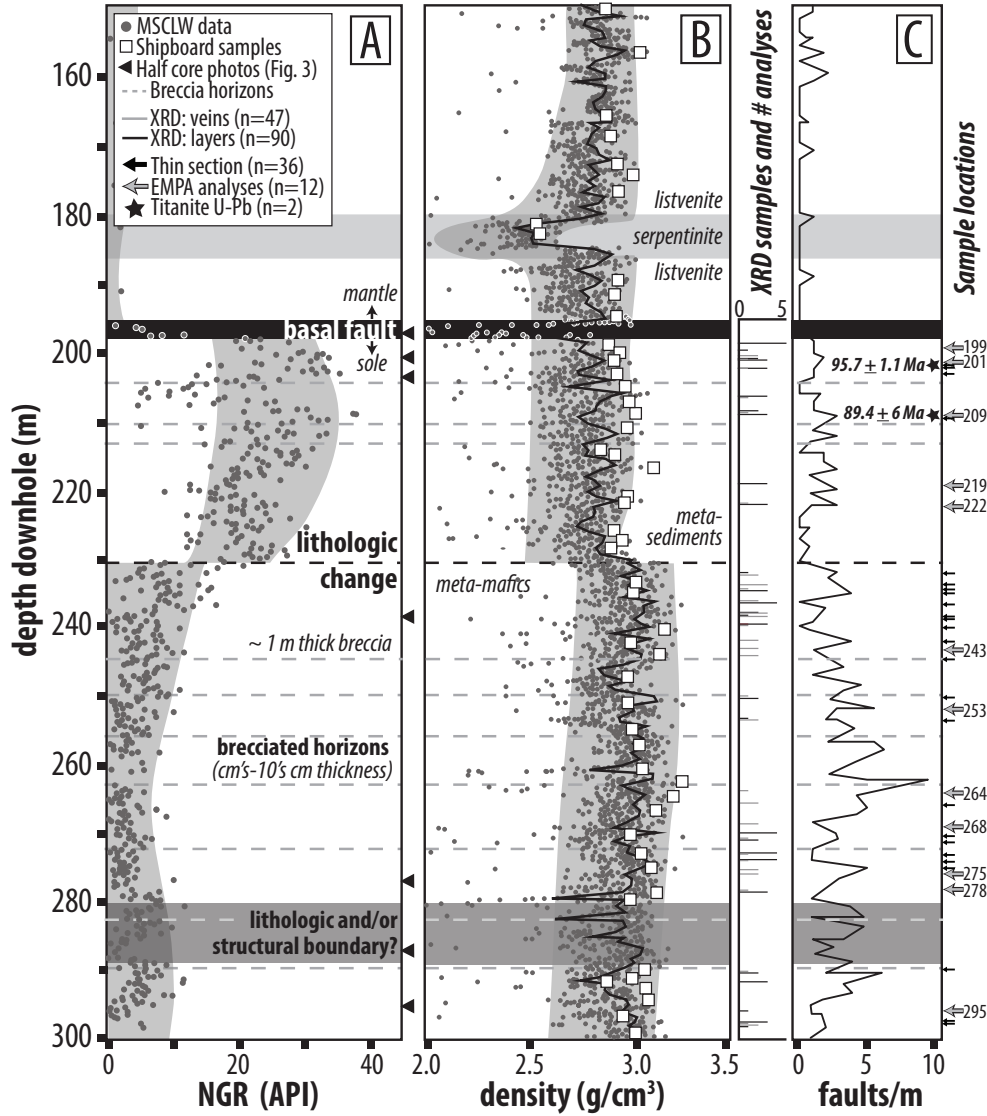


Figure 2: Down-hole trends in physical properties and structure for BT-1B from 150-300 m (bottom of the hole is 300 m). Depths and number of XRD analyses, thin sectioned samples, and samples analyzed via EMPA and/or U-Pb are indicated. Numbers next to sample depths are meters down-hole. Grey dots are from Multi-Sensor Core Logging of Whole-round cores (MSCL-W) and white squares in (B) are measurements from shipboard samples. Black triangles mark half core photos shown in Figure 3. (A) Natural Gamma Radiation (NGR) in American Petroleum Institute (API) units. (B) Density in g/cm³. (C) Down-hole abundance of brittle faults (mm-scale to cm-scale offset, normal and thrust sense) per meter. Dashed grey lines are brecciated horizons, cm's to 10's of cm thick.

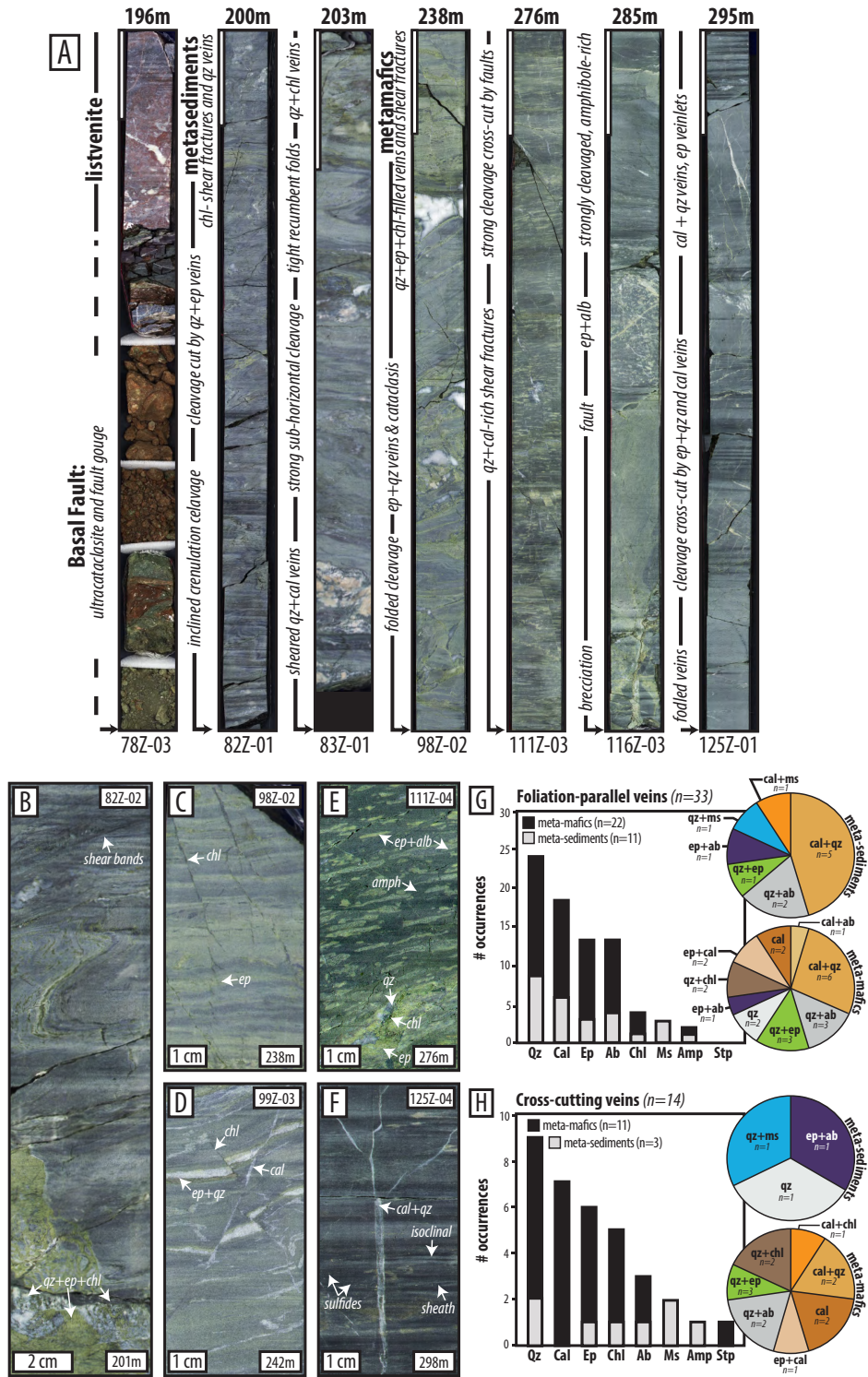


Figure 3: (A) Selected half core photos displaying the structural and lithologic variability in BT-1B. At the top of each photo, the starting depth is listed in meters down-hole. Vertical white bars are 10 cm. (B-F) Close-up half-core photos showing key structures and cross-cutting relationships in (B) meta-sediments (Section 1), (C-E) epidote-rich meta-mafics (Section 2), and (F) amphibole-rich meta-mafics (Section 3). (G,H) Histograms of XRD results showing foliation-parallel and cross-cutting vein mineralogy. Pie charts show the number of occurrences of specific mineral pairs, representing the two most abundant phases in polymineralic veins.

3.1 Mafic Geochemistry and Mineralogic Variations

Four meta-mafic samples were selected for bulk geochemical analysis. They have immobile trace element signatures characteristic of normal mid-ocean ridge and alkalic, “within-plate” basalts. This signature is different than the ophiolite lava chemistry (Fig. A1, Table A1), and comparable to compositions reported for other mafic metamorphic rocks of the HT sole (Searle & Cox, 2002).

To assess the nature of lithologic variations as inferred from color and textural differences, all visually distinct layers were sampled by micro-drilling for XRD analyses (Table A3). The common meta-sedimentary mineral assemblage (n=22) is dominated by muscovite, quartz, albite, titanite, hematite, and chlorite, with some layers containing detectable epidote, amphibole, apatite, calcite, and potentially stilpnomelane (n=1, but not confirmed with EMPA) (Fig. A2). The common meta-mafic mineral assemblage (n=68) is epidote, chlorite, albite, and calcic amphibole. Small amounts of muscovite, quartz, and titanite are common and some samples have detectable hematite, apatite, calcite, and potentially stilpnomelane (n=2, but not confirmed with EMPA) (Fig. A2).

3.2 Veinlets and Veins

Veinlets (<1 mm thick) and veins (up to ~1 cm thick) are abundant in the core. While some are cross-cutting and late in the deformation history, many are clearly folded and some appear to have been transposed. XRD analysis of foliation-parallel (n=33) and cross-cutting (n=11) veins reveal quartz, calcite, epidote, albite, and chlorite dominate, usually in bimineralic associations. Older foliation-parallel and probably transposed veins are dominated by calcite + quartz, quartz + albite, and quartz + epidote (Fig. 3G) while younger cross-cutting veins are more commonly monomineralic quartz or calcite (Fig. 3H). Veins in the meta-mafic rocks are combinations of quartz, calcite, epidote, albite and chlorite; these mineralogies are common in greenschist facies terranes. Most of these veins post-date peak conditions of metamorphism.

4 Deformation and metamorphism in the Low-Temperature sole

Thirty-six samples were collected from the metamorphic sole in the BT-1B core and examined petrographically (Fig. 2, black and grey arrows in panel C). Twelve samples, representative of the full range of metamorphic variations, were selected for optical microstruc-

tural study and quantitative Electron Microprobe Analyses (EMPA) (5 meta-sediments, 7 meta-mafics; grey arrows in Fig. 2C). Three deformation and metamorphic stages (D_{1-3}) were identified and described in terms of their dominant foliation- and lineation-forming mineralogy, mineral stability and kinematic context (pre-, syn-, post-kinematic with respect to surrounding fabric), breakdown and replacement textures, and whether metamorphism was dynamic (i.e., metamorphic growth in a preferred orientation) or static (i.e., randomly oriented growth). Samples containing large blue-green amphibole crystals (≥ 1 mm in length) were targeted for EMPA analyses at the University of Texas at Austin on the JEOL JXA-8200 in the Department of Geological Sciences (details in Appendix B and Appendix C).

D_1 and D_2 appear to record progressive development of prograde penetrative strain. A third, distinct stage of overprinting under lower temperature conditions was identified as deformation stage D_3 . Dynamic deformation and metamorphism and ductile fabric regeneration during D_1 and D_2 became progressively less penetrative during D_{3d} (d for ductile), and transitioned to a stage of brittle, less pervasive faulting and veining during D_{3b} (b for brittle).

4.1 D_1 and D_2 deformation and prograde greenschist to epidote-amphibolite metamorphism

4.1.1 *Microstructures*

No primary depositional or magmatic textures were observed in the phyllitic or meta-mafic units. Two stages of penetrative ductile strain are identifiable in most thin sections. In phyllitic meta-sedimentary rocks, the oldest stage, D_1 , developed a strong mica-rich foliation, S_1 . This foliation contains mm to 10's of cm scale layers that are rich in quartz + albite \pm epidote and/or calcite (Fig. 4A-F). Some foliation-parallel syn- D_1 compositional layering are quartz, quartz \pm albite, and quartz \pm epidote veins that were transposed parallel to the developing foliation and ductilely pinched (Fig. 4C). The S_1 fabric was folded during D_2 , which is best seen in deformed compositional layers and veins (Fig. 4A-C,F). D_2 folding varies in geometry from open, to tight, to isoclinal (Fig. 4A-D) and locally formed an S_2 axial planar cleavage that is sub-parallel to S_1 . S_2 is best developed in mica-rich layers (Fig. 4F). Locally, D_2 folding produced rootless fishhook and eye (sheath) structures, indicating that shear strain was large (Fig. 4A-D). The S_2 foliation contains syn-kinematic porphyroblastic

apatite (50-500 μm) and epidote with allanite cores (10-50 μm) fringed by albite pressure shadows (Fig. 4B), and titanite with white mica pressure shadows (Fig. 4E,F).

The schistose meta-mafic rocks record a similar D_1 and D_2 fabric evolution. The dominant foliation comprises alternating, mm's to cm's thick, epidote-albite and amphibole-epidote compositional layers (S_1 , Fig. 4G-M). The S_1 schistosity contains preferentially aligned blue-green amphibole, white mica, and chlorite that define a strong lineation (Fig. 4G-I, L-M) and contains fully transposed, syn- D_1 quartz, quartz \pm albite, and quartz \pm calcite veins, some of which exhibit ductile pinch-and-swell textures (Fig. 4I). S_1 was folded into open-to-tight and isoclinal microfolds during D_2 . D_2 locally developed an S_2 axial planar cleavage that is sub-parallel to S_1 . D_2 folding is best seen in relatively coarse-grained amphibole-rich layers (Fig. 4J). Amphibole porphyroblasts grew parallel (syn- D_1 and D_2) and oblique to the folded foliation; oblique blasts are syn- D_2 since they have inclusion trails of Fe-Ti oxides and white mica that are continuous with the external S_2 foliation (Fig. 4K). The S_2 foliation contains syn-kinematic porphyroblastic titanite (10-100 μm), and epidote with allanite cores (10-50 μm) (Fig. 4M). We did not find rutile in any of these rocks.

4.1.2 Mineral Chemistry

S_1 - and S_2 -forming white mica falls on a solid solution between muscovite and celadonite. K atoms per formula unit (apfu) are between 0.8-1.0 and paragonite component is ≤ 0.04 (Fig. C1). Si apfu are elevated with respect to ideal muscovite and span ~ 3.1 -3.3, approaching 'ideal phengite' (Fig. C1). There is no clear trend in Si apfu with depth in the core, but the deepest sample (222) is an intercalated mafic lens within the dominantly meta-sedimentary section, and contains mica with the highest measured Si apfu (~ 3.3 -3.6). White micas record differences in Si content corresponding to micro-structural context. The oldest foliation, S_1 , is characterized by Si apfu of ~ 3.2 -3.3 (Fig. 4D; C1B). Partially recrystallized mica defining the S_2 cleavage records higher Si apfu, ~ 3.35 -3.40 (Fig. 4D; C1B). EDS analyses confirm that S_1 and S_2 plagioclase is albite, with calcium content below detection.

Amphiboles defining the S_1 and S_2 foliations record core-to-rim zonations characterized by decreasing Mg#, decreasing Si apfu, and increasing Na/(Na+Ca) (e.g. Fig. 4H, L-M). This zoning was documented in samples 243, 253, 268, and 295 (Fig. 6A,B) and captures a change from actinolite or actinolitic-hornblende to magnesio-hornblende or edenite. Sample 243 is an exception; it has hornblende cores and pargasite rims (Fig. 6). Zonations are thin

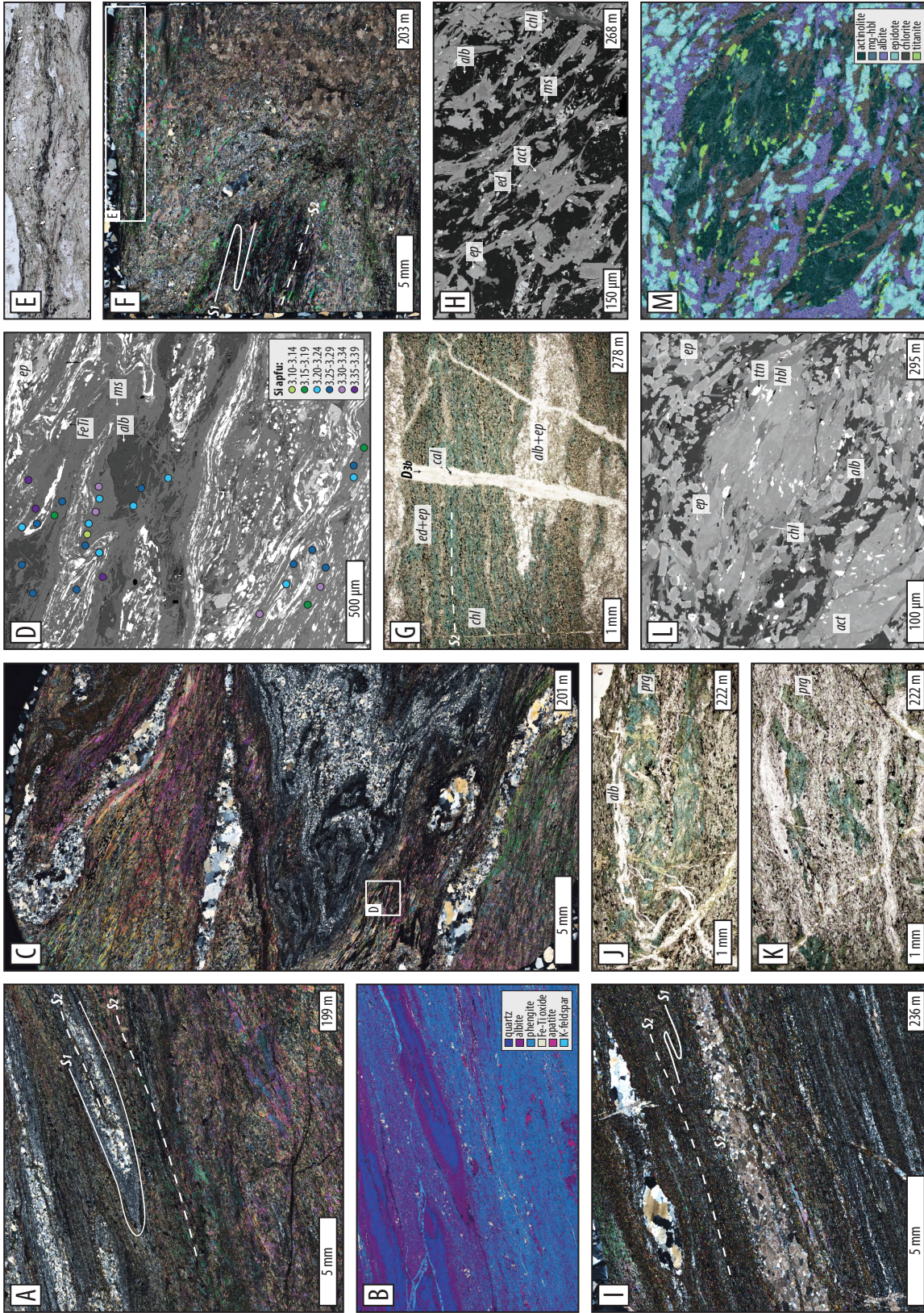


Figure 4: Representative photomicrographs of D1 and D2 microstructures in meta-sediments (A-F) and meta-mafics (G-M). Ductile foliations contain the axial planes of isoclinal folds (A-D, J), fish-hook and eye structures (A-D), and boudinaged and transposed veins (A, C, I). (D) BSE Image of area corresponding to white box in (C), with Si-in-phengite results shown. (E,F) Calc-phyllite sample (AK203) used for U-Pb geochronology; syn-kinematic D2 titanites are indicated by white arrows in (E). Amphibole zonation and chemistries (i.e. paragonite and magnesio-hornblende) defining S1 and S2 (e.g., G, H, J-M). Mineral abbreviations: act=actinolite, aln=allanite, alb=albite, chl=chlorite, ed=edenite, ep=epidote, FeTi=Fe-Ti oxide, hbl=hornblende, ms=muscovite, prg=paragonite, ttn=titanite.

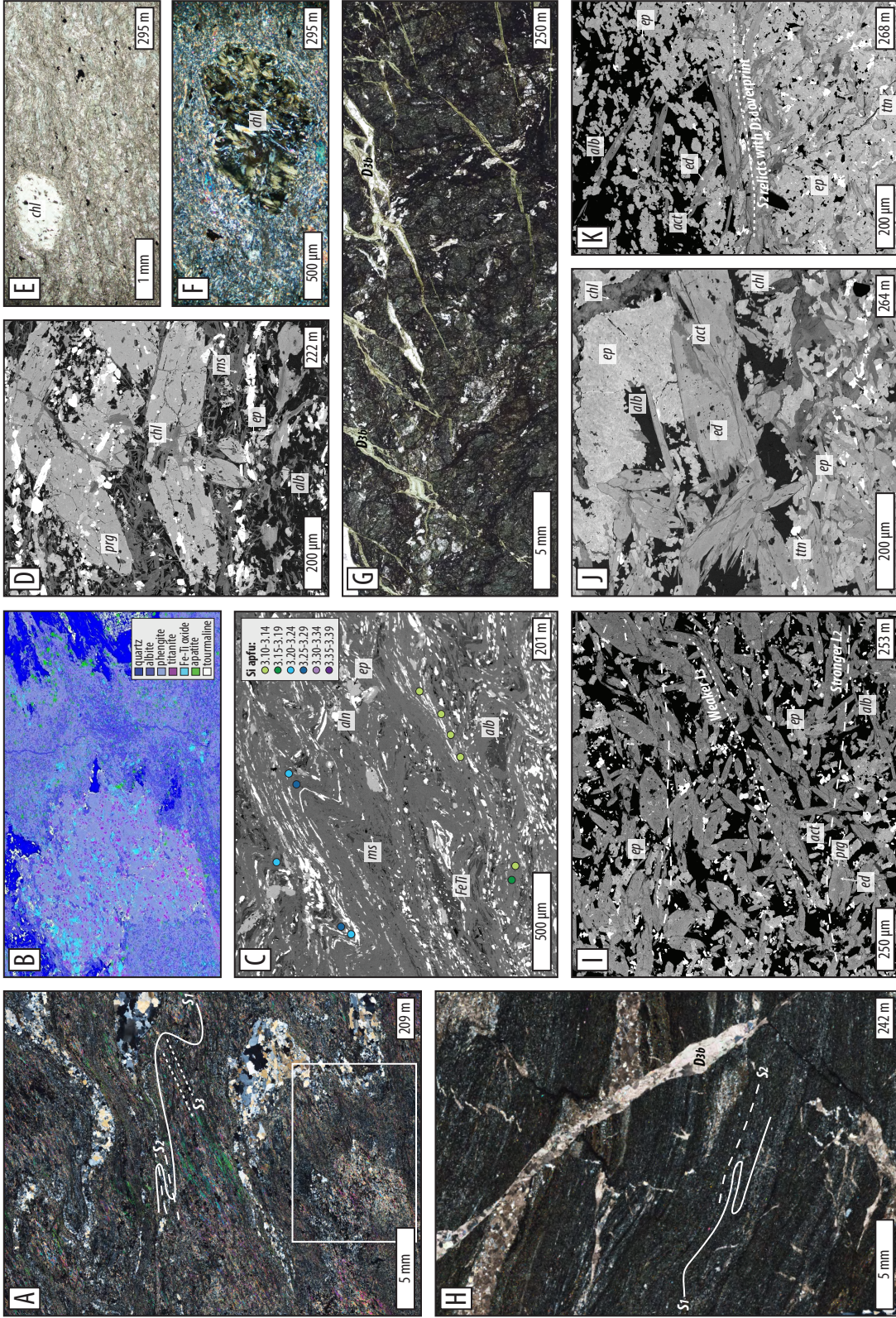


Figure 5: Representative photomicrographs of D3 microstructures in meta-sediments (A-C) and meta-mafics (D-K). S1 and S2 foliations are crenulated during D3, locally forming a new axial planar cleavage, S3 (A-C). (C) BSE image with Si-in-phengite results shown. (A,B) Quartz-albite-mica schist sample (AK209) used for U-Pb geochronology; syn-kinematic D3 titanites are shown in the false-colored X-Ray map in (B), corresponding to white box in (A). Chloritization during D3 manifests as foliation-parallel overgrowths and mineralized necks of brittle boudinaged amphibole (D), static pseudomorphing of garnet (?) (E,F), and cross-cutting veins (G). (H) Late cross-cutting veins contain calcite and record normal sense of shear. (I-K) D3 amphibole zonations overprint the S2 foliation. Mineral abbreviations: act=actinolite, alb=albite, aln=allanite, chl=chlorite, ed=edenite, ep=epidote, FeTi=Fe-Ti oxide, hbl=hornblende, ms=muscovite, prg=paragonite, ttn=titanite.

or absent on the tops of elongate crystals, indicating enhanced dissolution perpendicular to foliation, and are thicker parallel to lineation (Fig. 4M). No zoning was found in samples 222 and 278 the homogeneous grains of S_1 - and S_2 -forming amphibole are (ferro-) pargasite and (ferro-) edenite, respectively (Figs. 4G,J; 6). In sample 222, S_1 -defining blue-green pargasite is stable during D_2 folding, and S_2 contains syn-kinematic unzoned pargasite (Fig. 4J,K).

Maximum Al_2O_3 in S_2 -defining amphiboles decreases with depth in the core, from ~ 13 -15 wt% between ~ 196 -230 m, to ~ 10 -13 wt% between ~ 230 -300 m (Fig. 7A). Maximum Al_2O_3 in sample 295 is also ~ 10 wt%, but these rims are distinct from other samples because they have $(Na+K)_A < 0.5$ (similar to 268 cores). Maximum TiO_2 drops markedly across the ~ 280 -290 m horizon from ~ 0.4 wt% to ~ 0.25 wt% (Fig. 7B).

4.2 D_3 deformation and retrograde greenschist metamorphism

4.2.1 Microstructures

In meta-sedimentary rocks in the upper 34 m of the core, the S_2 foliation was re-folded producing D_3 crenulations (Fig. 5A,C). Locally, mica-rich layers developed strong S_3 cleavages that are parasitic to axial planes of larger, cm-scale folds visible in thin section (Fig 5A-C). D_3 crenulations contain pre-to-syn-kinematic titanite porphyroblasts (~ 30 -300 μm) that have rotated into alignment with the S_3 cleavage (Fig 5B), suggesting that crystals continued growing during D_3 .

D_3 crenulations do not manifest clearly in meta-mafic rocks. The best evidence for folding are several changes in apparent dip direction of the meta-mafic S_2 foliation with depth down-core. In most samples, amphibole porphyroblasts define one strong and one weak lineation, potentially recording the older S_2 and a younger, weak S_3 fabric, respectively. The younger, weaker fabric is reported herein as D_{3d} (d for dutile) (Fig. 5I-K). Syn-kinematic amphibole zonations support the inference that deformation continued under P-T conditions different than D_2 (chemistry discussed below). Where the S_2 foliation records the best evidence of a D_3 overprint, it occurs as lineation-parallel green amphibole and dynamic chlorite rims replacing amphibole. D_3 chlorite also grew in brittle micro-boudin necks dissecting amphibole porphyroblasts (Fig. 4M, 5D), and formed patchy replacement textures and static pseudomorphs of what might have been garnet in one sample (Fig. 5D-G; no pristine garnet was found).

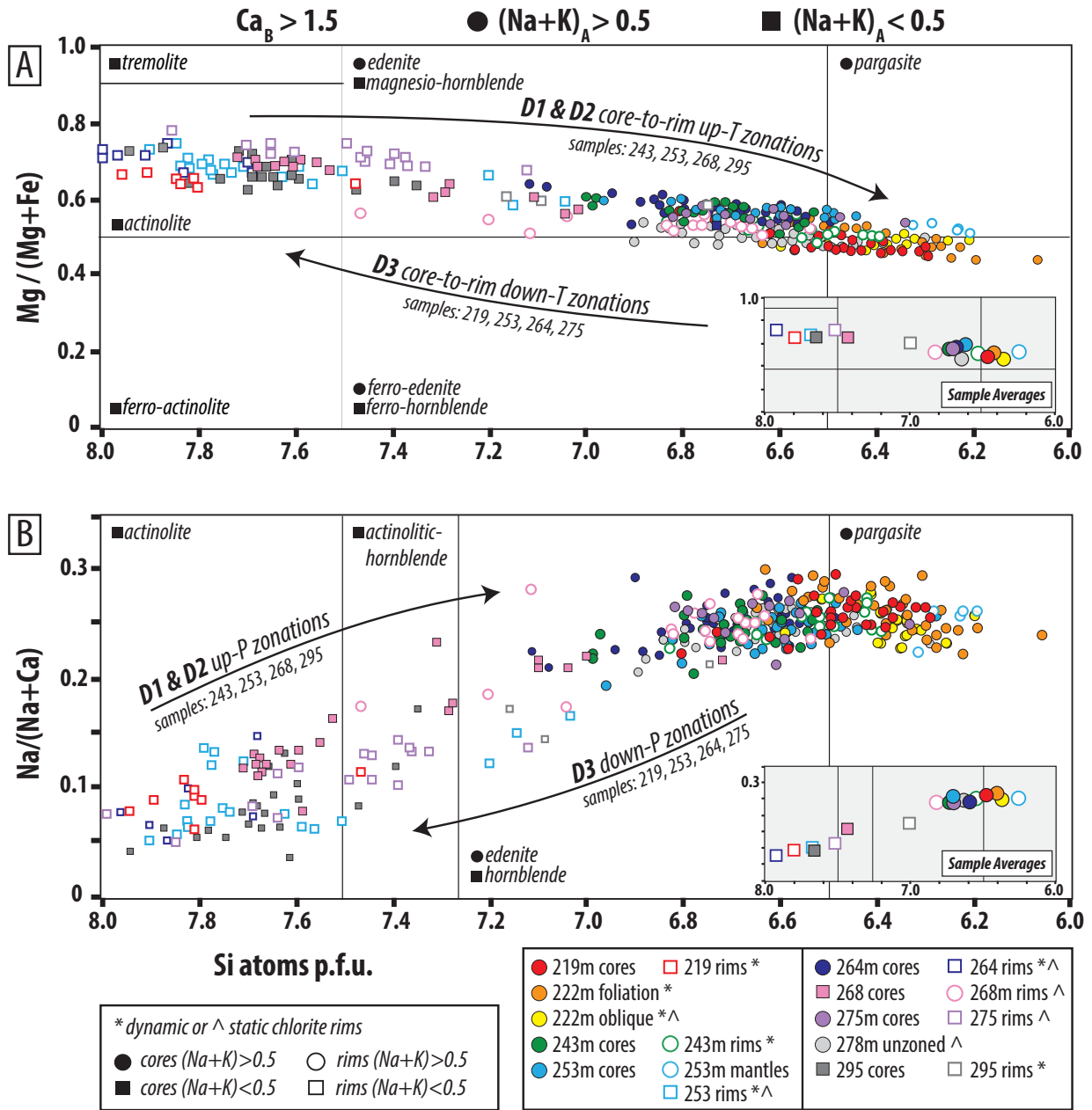


Figure 6: EMPA amphibole analyses. Circles indicate $(\text{Na}+\text{K})_A > 0.5$, and squares indicate $(\text{Na}+\text{K})_A < 0.5$. Filled symbols are cores, open symbols are rims. (A) Si atoms p.f.u. vs. Mg#. (B) Si atoms p.f.u. vs. Na/(Na+Ca). Fields are labeled according to Leake et al. (1997) classification. Data are colored by depth down-hole, with warmer colors corresponding to shallower depths. Black arrows indicate trends from core-to-rim for samples listed, corresponding to progressive deformation as indicated. Sample averages for cores and rims are shown in the grey inset boxes.

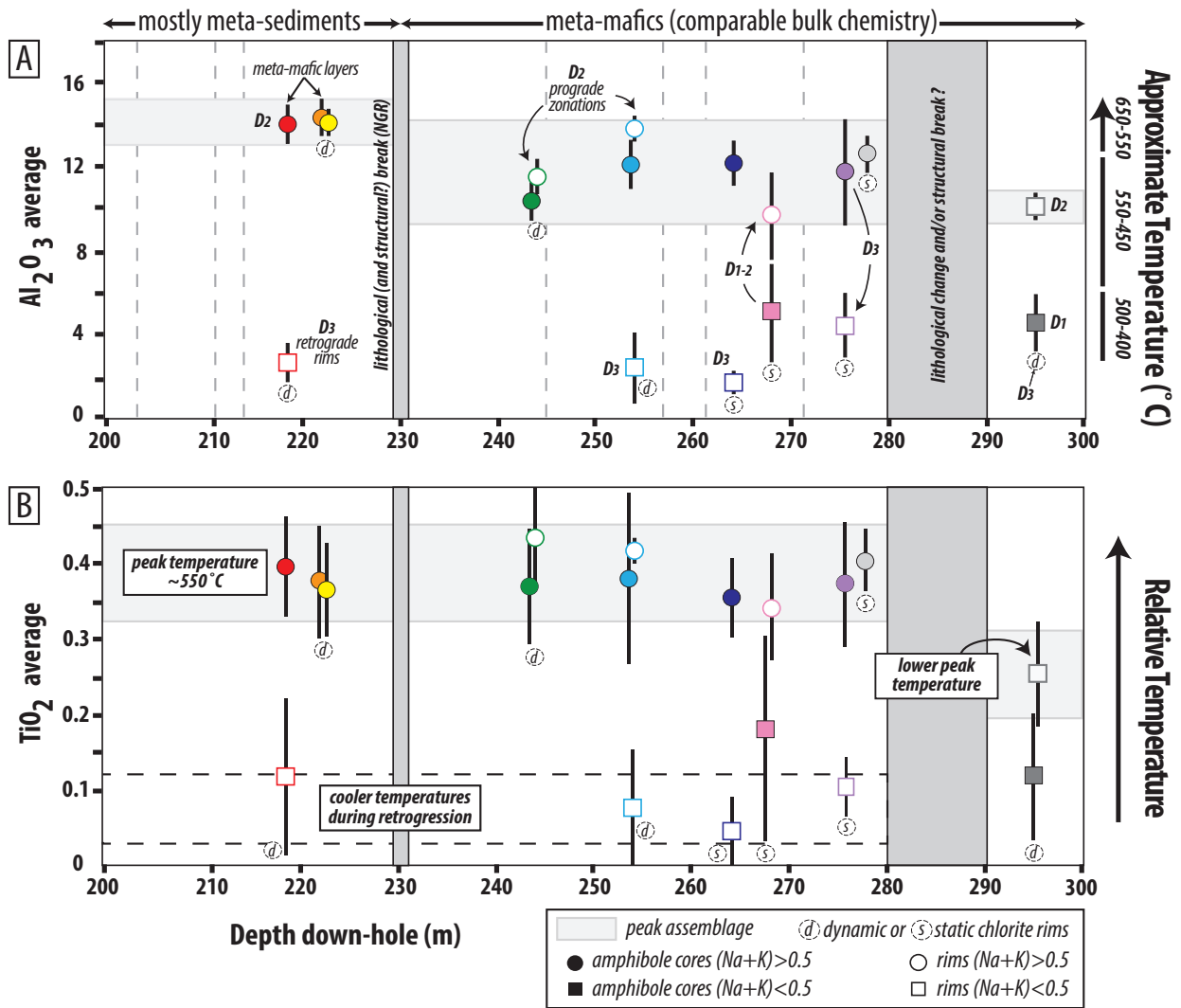


Figure 7: Downhole trends in amphibole chemistry. Vertical dashed grey lines in (A) are brecciated horizons. Samples with dynamic and static chlorite rims are marked as indicated. (A) Maximum Al_2O_3 and (B) TiO_2 in syn-D₂ amphiboles decrease slightly with depth. Actinolite overgrowths record D₃ retrogression.

During D_3 in all rock types, S_2 was locally cross-cut by veins, micro-faults, thin zones of cataclasis, and brecciation (i.e. D_{3b} , b for brittle) (Fig. 3, 4G, 5G,H). Millimeter- to cm-scale thrust-sense chloritized micro-faults occur through much of the meta-mafic section (e.g. Fig. 3C,D) and are cross-cut by normal-sense, calcite-filled micro-faults and veinlets that offset S_2 and D_{3b} chlorite-filled thrust faults (Fig. 3D,F; 5H).

4.2.2 Mineral Chemistry

White micas defining D_3 fabrics have lower Si contents than D_1 and D_2 fabrics. Where S_{1-2} cleavages are preserved in crenulation hinges, they preserve higher Si contents (3.2-3.3 apfu), but where the D_3 crenulation forms a strong S_3 cleavage, Si contents are reduced to 3.10-3.15 apfu (Fig. 5C, C1B).

Amphiboles that define the syn- D_{3d} overprint of the S_2 foliation record core-to-rim zonations characterized by increasing Mg#, increasing Si apfu, and decreasing Na/(Na+Ca) (e.g. Fig. 5I-K). This zoning was documented in samples 219, 264 and 275 (Fig. 6A,B) and corresponds to a change from pargasite or edenite to actinolite. Similar to D_{1-2} zonations, D_{3d} amphibole zonations developed as the fabric was continuously reworked. Thicker metamorphic rims grew in the lineation direction (Fig. 5J,K). Sample 253 is unique in that it both kinds of zoning are present; edenite cores grade to lower Mg#, higher Na-content pargasite mantles, and then to higher Mg#, higher Si, lower Na-content actinolite rims (Fig. 5I; 6). Actinolite is commonly in textural equilibrium with foliation-parallel D_{3d} chlorite, but in several samples chlorite occurs only as patchy replacement textures and static overgrowths (stars vs. carrots in the key in Fig. 6). D_{3d} actinolite rims have consistently low Al_2O_3 and TiO_2 of $\sim 2-4$ wt% and $\sim 0.05-0.1$ wt%, respectively, regardless of sample depth (Fig. 7A,B).

5 LA-ICP-MS titanite U-Pb geochronology

Titanite is a common accessory phase in many meta-mafic HP/LT rocks, including the sole rocks of Oman, and crystallizes over a wide range of prograde and retrograde P-T conditions. Although titanite has relatively low U (<10 ppm in metabasic rocks is common) and Th and high common Pb (Pb_c) contents compared to zircon, it has long been utilized as a successful U-Pb geochronometer (e.g., Frost et al., 2001; Kohn, 2017; Garber et al., 2017; Yakymchuk et al., 2017). Empirical and experimental titanite U-Pb closure temperature

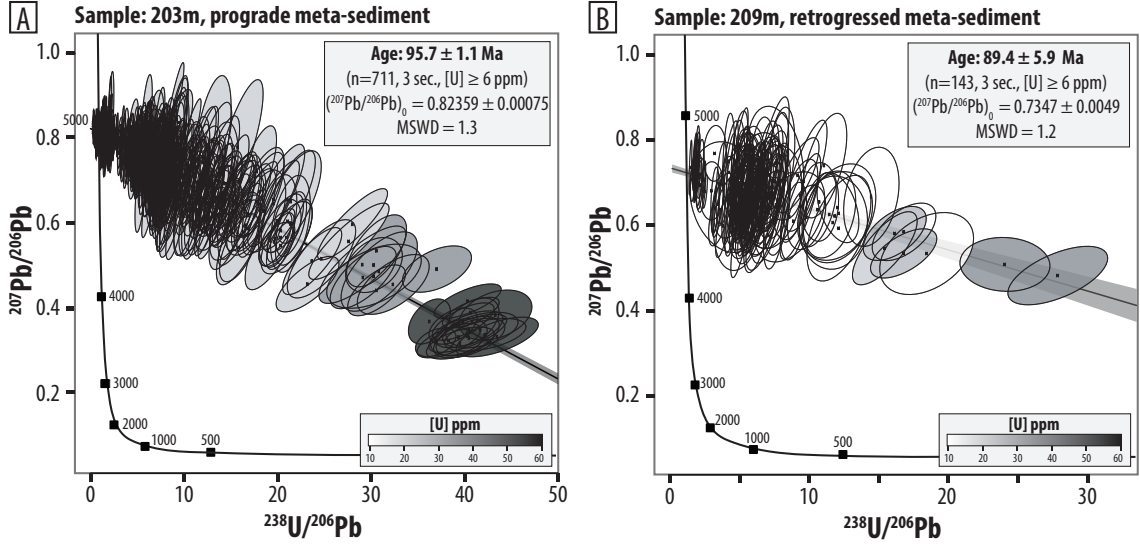


Figure 8: Results of titanite U-Pb for calc-schists plotted in Tera-Wasserburg space. (A) Sample AK203; and (B) sample AK209. Total number of data points, n , is the total number of 3-second increments with $[\text{U}] \geq 6$ ppm, for ~ 125 and 85 analyzed grains, respectively.

estimates vary dramatically from $\sim 600^\circ\text{C}$ to $>800^\circ\text{C}$ (e.g., Mezger et al., 1991; Cherniak, 1993; Kohn & Corrie, 2011; Spencer et al., 2013). However, metamorphic titanite growth appears to occur over a large temperature range, and both while temperature increases and decreases, well below proposed closure temperatures. Therefore, titanite U-Pb ages in HP/LT rocks can date titanite growth and be interpreted in their proper microstructural context to provide critical insights into the timing of deformation and metamorphism.

In light of the low U and variable Pb_c content, LA-ICP-MS U-Pb analyses of titanite may be hampered and the precision limited, as they do not yield concordant ages. The variable Pb_c content or $[\text{U}]$, however, can be leveraged in Tera-Wasserburg space to define inverse isochrons (i.e., mixing trajectories between radiogenic and common Pb). While ages can be calculated assuming a Stacey and Kramers (1975) model Pb composition, it is far more strategic to leverage internal titanite U and Pb variability to define more robust regressions and deriving lower-intercept ages without making model Pb composition assumptions. Traditionally, studies use different bulk titanite spot analyses to regress intercept ages and Pb_c composition, but for this study, we utilized a depth-profiling approach to resolve intra-grain U and Pb_c variations and to refine lower intercept age precision. We subdivided the continuous 30 sec ablation trace into 3-sec ($\sim 2 \mu\text{m}$) segments to capture the variability in U and Pb_c and regressed these 3-sec U-Pb analyses (cf. Odlum & Stockli, 2019).

LA-ICP-MS titanite U-Pb data were collected from the two meta-sedimentary calc-
 phyllite samples that contained the largest and most abundant titanite. Grains were an-
 alyzed in-situ on $\sim 30 \mu\text{m}$ thin sections in order to retain the micro-textural context of
 porphyroblasts, which allowed us to interpret ages in the context of progressive deformation
 (Figs. 4E,F; 5A,B). Samples were analyzed at the University of Texas at Austin UTChron
 Laboratory using a 193nm ArF Excimer laser ablation system with a Helex cell coupled to
 an Element 2 HR-ICP-MS. Titanite were ablated using 30 or 60 μm spot sizes for 30 sec
 at 10Hz with an energy of 4 mJ. OTL-1 was used as primary titanite standard (1015 ± 2
 Ma; Kennedy et al. (2010)) and interspersed every 4 unknown analyses for elemental and
 depth-dependent fractionation. BLR-1 (1047 ± 0.4 Ma; Aleinikoff et al. (2002), Bonamici et
 al. (2015)) was used as a secondary standard for quality control. No common ^{204}Pb correc-
 tion was applied due to the interference with ^{204}Hg in the He and Ar gases. Data reduction
 was performed using the IgorPro (Paton et al., 2010) based Iolite 3.4 software with Visual
 Age data reduction scheme (Petrus & Kamber, 2012). All bulk and 3-sec data are given at
 2-sigma with internal and external uncertainty propagated. Data were regressed and lower
 intercept $^{206}\text{Pb}/^{238}\text{U}$ ages were calculated using IsoplotR (Vermeesch, 2018).

Sample 203 is a quartz-mica coarsely phyllitic calcareous layer that displays a strong
 D_2 fabric. The S_2 cleavage is well-developed in white mica and Fe-Ti oxide-rich lenses and
 is axial planar to cm-scale folds (Fig. 4E,F). Subsequent warping of the D_2 foliation is
 evident in small crenulations that kinked mica, and locally rotated titanite (Fig. 4E) but
 this deformation was not penetrative. Titanite blasts are syn- D_2 as evidenced from their
 fish-shaped geometries. About 125 grains were analysed and the data were regressed as
 3-second increments and filtered for $[\text{U}] \geq 6$ ppm. In Tera-Wasserburg space, 711 datapoints
 yielded a lower-intercept age of 95.7 ± 1.1 Ma (MSWD = 1.3; Fig. 8A).

Sample 209 is a quartz-calcite-mica phyllite that records evidence for D_{3d} . The strong
 S_2 isoclinally-folded foliation was refolded into tight D_{3d} folds, producing an axial planar S_3
 cleavage in white mica and albite-rich layering (Fig. 5A). Fe-Ti oxide, apatite and titanite
 porphyroblasts, and quartz-rich microlithons define D_{3d} microfolds (Fig. 5B). Most titanite
 blasts are aligned parallel to the S_3 cleavage (Fig. 5B). About 85 grains were analyzed;
 data were regressed in 3-second increments and filtered for $[\text{U}] \geq 6$ ppm. In Tera-Wasserburg
 space, 143 datapoints yielded lower-intercept age of 89.4 ± 5.9 Ma (MSWD = 1.2; Fig. 8B).
 The lower precision compared to sample 203 is mainly related to lower U content.

6 Interpreted tectonic context, P-T conditions, and timing of deformation and metamorphism in the LT sole at Site BT-1B

Since there are no significant differences in major element chemistry between the four meta-mafic samples that were analyzed (cf. Table A1), we interpret the differences in amphibole composition to reflect changes in P and T during deformation. The structural petrology and geochronology data presented above demonstrate that D₁ and D₂ developed during prograde-to-peak subduction, and penetrative ductile deformation occurred under epidote-amphibolite facies conditions at ~95-96 Ma. D₃ developed as mechanical behavior changed from pervasively ductile strain to increasingly localized brittle behavior as retrograde temperatures lowered to greenschist facies conditions at ~90 Ma. D₃ is concurrent with the initial stages of exhumation, which we interpret to have occurred along the top of the subduction channel shear zone. During the deformation progression from D₁₋₃, older veins were transposed into foliation parallel layering, and cross-cut by later veins, indicating that the high fluid pressure conditions required for extension fracturing was present, at least transiently, during prograde and retrograde metamorphism. Greenschist overprinting did not completely wipe out evidence of syn-subduction prograde-to-peak conditions, and carbonate minerals are volumetrically minor, indicating that the water flux and CO₂ content were limited, respectively.

6.1 Evolving conditions and timing of prograde metamorphism

During D₁₋₂, S₁ and S₂ developed as P and T increased during subduction. Phengitic white mica records increasing Si apfu during S₂ cleavage development, indicative of increasing pressure conditions (Fig. 9). Experimental calibration of the phengite geobarometer was performed with coexisting K-feldspar, quartz, and phlogopite (Velde, 1965; Massonne & Schreyer, 1987; Massonne & Szpurka, 1997). In the absence of these buffering phases, the experimental calibration can only be used to estimate minimum pressures in the presence of a Mg-Fe silicate (cf. Massonne & Schreyer, 1987). In sample 222, Mg-Fe amphibole is a foliation-forming phase, and S₂-defining phengite records ~3.5 Si apfu, indicating D₂ occurred at minimum pressures of ~8-12 kbar for temperatures of ~400-600°C (Fig. 9). The other phengite data (samples 199, 201 and 209) come from meta-sedimentary phyllites that contain neither a buffering mineral assemblage nor a co-existing Mg-Fe silicate. In those samples, S₁ and S₂ schistosity record a tight data cluster of ~3.1-3.3 apfu. As there are no obvious structural discontinuities within the 34 m thick meta-sedimentary section, it

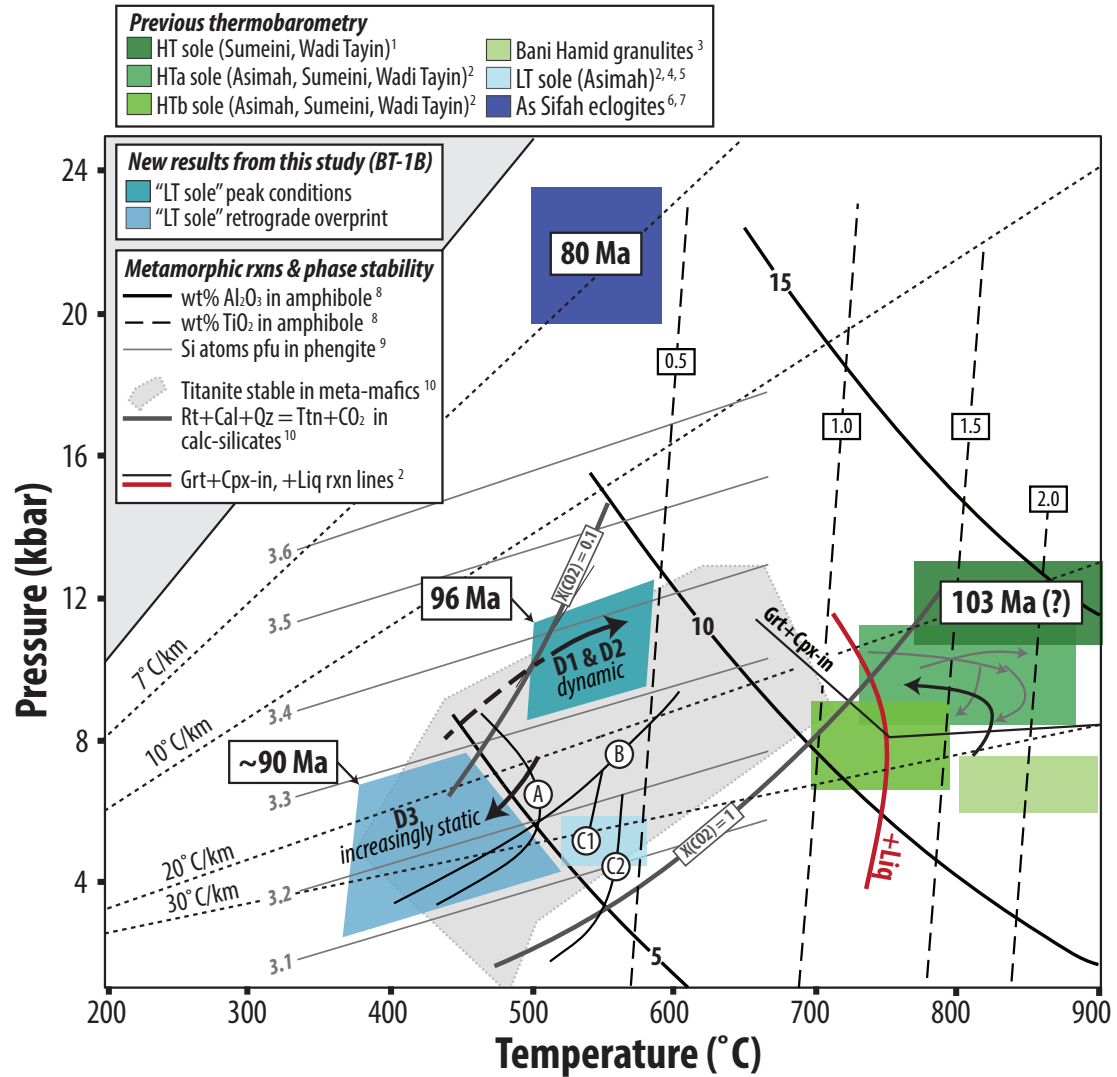


Figure 9: Estimated P-T conditions and timing of metamorphism in the LT sole in core BT-1B (teal colors), compared with the HT sole (green) and As Sifah eclogites (dark blue) in NE Oman. Grey P-T trajectories for the HT sole are from Soret et al. (2017); black counterclockwise trajectory is from Hacker (1991). References: (1) Cowan et al. (2014), (2) Soret et al. (2017), (3) Searle et al. (2015), (4) Gnos (1998), (5) Bucher (1991), (6) Wendt et al. (1993), (7) Searle et al. (1994). Contours for wt% Al₂O₃ and TiO₂ in amphibole from (8) Ernst and Liu (1998). Contours for Si atoms p.f.u. in white mica from (9) Massonne and Schreyer (1987). Titanite stability in meta-mafic rocks and calc-silicates (for end-member fluid compositions) from (10) Kohn (2017). Metamorphic reactions: (A) actinolite-hornblende and (B) albite-oligoclase transitions after Maruyama et al. (1983); (C) Chl+Ttn+Qz+Act = Hbl+Ilm+fluid, buffered by (1) nickel-nickel-oxide and (2) quartz-magnetite-fayalite after Liou et al. (1974); (D) Ep+Hbl_I+Qz = Hbl_{II}+Olig+fluid after Apter and Liou (1983). Ages of metamorphism are from Guilmette et al. (2018) (HT sole), this study (LT sole), and Warren et al. (2005) (As Sifah).

appears this portion of the core, while highly sheared, reached roughly the same depths of burial at the culmination of D₂ ($\geq 8-12$ kbar).

S₁ and S₂-defining amphibole evolved from actinolite to magnesio-hornblende/edenite, or edenite to pargasite. The exact core-to-rim evolution and type of amphibole that grew was likely a function of local differences in reactive bulk composition and strain. Rare actinolite cores, observed in 2 of 9 meta-mafic samples analyzed, preserve evidence for prograde subduction through greenschist facies conditions (Fig. 9; 268 m and 295 m), but most samples appear to have fully equilibrated at lower amphibolite facies conditions. At the greenschist-to-amphibolite facies transition, Al₂O₃ in Ca-amphiboles (i.e. Ca_B > 1.5, all samples analyzed) increases from ~5-15 wt% (Apted & Liou, 1983; Ernst, 1988), TiO₂ surpasses ~0.5 wt% (Ernst, 1988), and Mg/(Mg+Fe) and total Ti, Na and K contents increase while Si decreases (cf. Fig. 6) (e.g., Shido & Miyashiro, 1959; Raase, 1974; Holland & Richardson, 1979; Laird & Albee, 1981). Peak P-T during D₂ are constrained using empirical data from other metamorphic terranes with reported P-T estimates from experimental petrology data (Holland & Richardson, 1979; Laird & Albee, 1981; Blundy & Holland, 1990; Holland & Blundy, 1994; Ernst & Liu, 1998). The maximum values of Al₂O₃, TiO₂, and (Na+K) apfu in syn-D₂ amphibole zones are consistent with metamorphism at ~8-12 kbar and ~400-550°C (Fig. 7, 9, C2). The lack of rutile indicates P < 15 kbar. Maximum T of ~550°C is well-constrained by amphibole Ti-contents and is consistent with Raman spectroscopy on carbonaceous material (Soret et al., 2017). The absence of oligoclase, which replaces albite above the peristerite gap, also indicates T < 600°C (Maruyama et al., 1982). Core and rim analyses shows that most amphiboles record the retrograde D₃ progression to actinolite composition. The exceptions are samples 268 and 278. In sample 268, cores are actinolite and rims are edenite. In sample 278, no zonations were observed with amphibole being homogeneous edenite. Both samples appear to record prograde metamorphism, and local late static chloritization.

In the meta-mafic section, maximum Al₂O₃ and TiO₂ values in amphibole (interpreted as indicators of peak P and T, respectively) show a slight decrease with depth down the BT-1B core (Fig. 7). Changes in inferred maximum T are not continuous as expected for conductive cooling across a shear zone (e.g. Gnos & Peters, 1992), but rather occur as stepwise changes, suggesting the cored BT-1B section comprises several distinct interface slices (cf. Soret et al., 2017). This is qualitatively supported by the observation of three petrologically distinct sub-sections in the core described above, comprising upper meta-

sedimentary phyllites (Section 1), a middle epidote-rich meta-mafic section (Section 2), and a lower amphibole-rich meta-mafic portion (Section 3). The upper portion of the core (Section 1) appears to have reached slightly higher P (Fig. 7A) but similar peak T (Fig. 7B) to middle Section 2, which could reflect increasing P along a dipping, roughly slab-parallel $\sim 500^\circ\text{C}$ isotherm (illustrated schematically in Fig. 10C). Even though the Al-content in sample 295 (Section 3) is similar to the middle section samples, lower (Na+K) and TiO_2 values than the rest of the core suggest lower peak T (cf. Laird & Albee, 1981; Ernst & Liu, 1998; Spear, 1995). This could indicate the bottom of the core occupied a structurally deeper position within the shear zone or was subducted later. For comparison, HT sole rocks also record a decrease in Ti-in-amphibole with structural depth away from the peridotite mantle, from ~ 2.3 to ~ 1.0 wt% TiO_2 (Ghent & Stout, 1981; Gnos, 1998; Searle & Malpas, 1982; Cowan et al., 2014; Soret et al., 2017). Soret et al. (2017) cited this observation as evidence for ‘tectonic slicing’ during subduction.

Abundant titanite and lack of rutile in D_{1-2} fabrics confirms deformation and metamorphism occurred under moderate P-T conditions in the presence of H_2O -rich, low- CO_2 fluids (Fig. 9; Kohn (2017)). In light of titanite’s relatively high U-Pb closure temperature ($>600^\circ\text{C}$), its proclivity to participate in metamorphic reactions over a wide range of P-T space (Frost et al., 2001; Kohn, 2017; Yakymchuk et al., 2017), and our new petrological constraints confirming peak temperatures in the LT sole of $<550^\circ\text{C}$, we interpret the syn- D_2 titanite U-Pb age from sample 203 to record the timing of titanite crystallization and S_2 cleavage development at ~ 96 Ma under epidote-amphibolite facies conditions.

6.2 Conditions and timing of exhumation

During D_3 , deformation and metamorphism continued as P and T decreased from epidote-amphibolite to greenschist facies conditions. Phengitic white mica recrystallized along S_3 cleavages; lower Si apfu values in S_3 micas relative to low-strain relicts of older fabrics preserved in micro-fold hinges indicate lower pressures during D_3 . D_3 retrogression overprinted S_2 and manifested as foliation- and lineation-parallel actinolite rims fringing pargasite or edenite cores and growth of foliation-forming chlorite, reflecting hydration reactions during cooling and decompression under greenschist facies conditions.

Metamorphic conditions of the ductile D_3 greenschist facies overprint are not sufficiently quantified to constrain the retrograde P-T path. The low Al and high Si contents

of actinolite do not meet calibration requirements for amphibole-plagioclase thermometry or Al-in-amphibole barometry (e.g. $\text{Al} \geq 0.5$ apfu and $\text{Si} \leq 7.8$ apfu). However, Al_2O_3 contents are consistently below 5 wt% and by analogy with other locations this suggests ~ 4 -7 kbar and 350-450°C (Fig. 9). TiO_2 values in retrograde actinolite are also similar regardless of sample depth. These observations suggest that, except for the lower ~ 10 m of the BT-1B core (represented by sample 295), the middle ~ 60 m thick section of meta-mafic rocks exhumed along similar P-T paths (Fig. 10D). Therefore, even if the uppermost meta-sedimentary section reached somewhat greater depths during subduction, most of the meta-mafic section seemingly behaved as a coherent unit during exhumation.

Titanite growth during decompression is common in subducted rocks, as evidenced in many HP/LT terranes by lineation-parallel overgrowths on rutile, and can efficiently redistribute high-field strength elements (Lucassen et al., 2010). We interpret the titanite U-Pb age from sample 209 to record syn- D_3 titanite growth during exhumation at ~ 90 Ma. The relatively large uncertainty for the age in part reflects the low U content but might also reflect the protracted nature of D_3 . Furthermore, as titanite should be reactive along the entire inferred P-T trajectory for the LT sole, the higher age uncertainty might also indicate the presence of older intergrown syn- D_2 titanite during protracted (re-)crystallization of syn- D_3 titanite.

Metamorphism became increasingly static and deformation increasingly brittle during D_3 decompression and cooling. Ductile fabrics were cross-cut first by D_{3b} reverse-sense brittle faults under hydrous conditions as evidenced by growth of chlorite, and later by D_{3b} normal-sense brittle faults associated with the influx of CO_2 -rich fluids that led to precipitation of calcite in veins (cf. Fig. 3D). Younger normal-sense micro-faults decorated with calcite could indicate that some exhumation occurred by brittle extension *after* underthrusting of the Arabian continental margin. Some CO_2 -rich fluids could have been sourced locally from calcareous strata in the metasedimentary section or from the underlying carbonate platform sediments (cf. de Obeso et al., 2018).

6.3 On the relative timing of listvenite formation

The source of CO_2 -rich fluids responsible for extensive listvenitization reactions in the overlying mantle peridotite section, and the timing and mechanisms of mass transfer, are matters of major scientific interest. While some workers have proposed that CO_2 was

derived from the metamorphic sole as is present in BT-1B (Lafay et al., 2019), this inference is not supported by our structural and petrologic observations. Several billion metric tonnes of CO_2 are required for near-complete carbonation of several km's thick peridotite mantle (Kelemen et al., 2011; Kelemen & Manning, 2015). However, the volume of carbonate in the sub-ophiolite metamorphic rocks present in BT-1B is minimal ($<1\%$) and typically localized to discontinuous veinlets and thin carbonate-rich layering metamorphosed into calc-phyllite. An abundance of titanite in calcite-bearing metasedimentary rocks implies extremely high $X_{\text{H}_2\text{O}}$ fluids (Kohn, 2017) during both subduction and exhumation since even a small component of CO_2 in a fluid would have stabilized rutile with calcite. Furthermore, Sr isotopic values of BT-1B sub-ophiolite metamorphic rocks are very different from Sr signatures of the overlying listvenitized mantle, but the listvenite mantle *is* isotopically similar to the underthrust unmetamorphosed Hawasina sedimentary strata (de Obeso et al., 2018). Together these observations indicate that the calcite-filled brittle micro-faults in the BT-1B metamorphics formed prior to tectonic juxtaposition of the metamorphic sole with the ophiolite along the Basal Fault. Thus, listvenitization occurred sometime before juxtaposition with the metamorphic sole sampled in the BT-1B core. We conclude that the metamorphic sole rocks in the BT-1B core were not the source of CO_2 for mantle carbonation.

The Basal Fault exposed in the BT-1B core is a ~ 40 cm thick brittle cataclastic zone. The sense and amount of offset across the zone is unknown, but the metamorphic rocks in the core record small-scale normal offsets suggestive of roughly horizontally-directed extensional deformation. As these rocks were not the source of the CO_2 that listvenitized the overlying mantle rocks, significant km-scale displacement is plausible to explain the mantle-sole juxtaposition present in the BT-1B core.

7 Discussion and Implications

7.1 Reappraisal of the tectonic significance of the LT sole

The LT sole is commonly envisioned as a section of the down-going slab that subducted at the same time as the HT sole, but was accreted at shallower depths. Our petrological analysis paints a contrasting picture and leads us to conclude that this LT sole section reached similar pressures and depths as the HT sole (~ 30 km), but experienced $\sim 300^\circ\text{C}$ colder peak temperatures. Furthermore, our new titanite U-Pb data indicate that this occurred at ~ 95 -

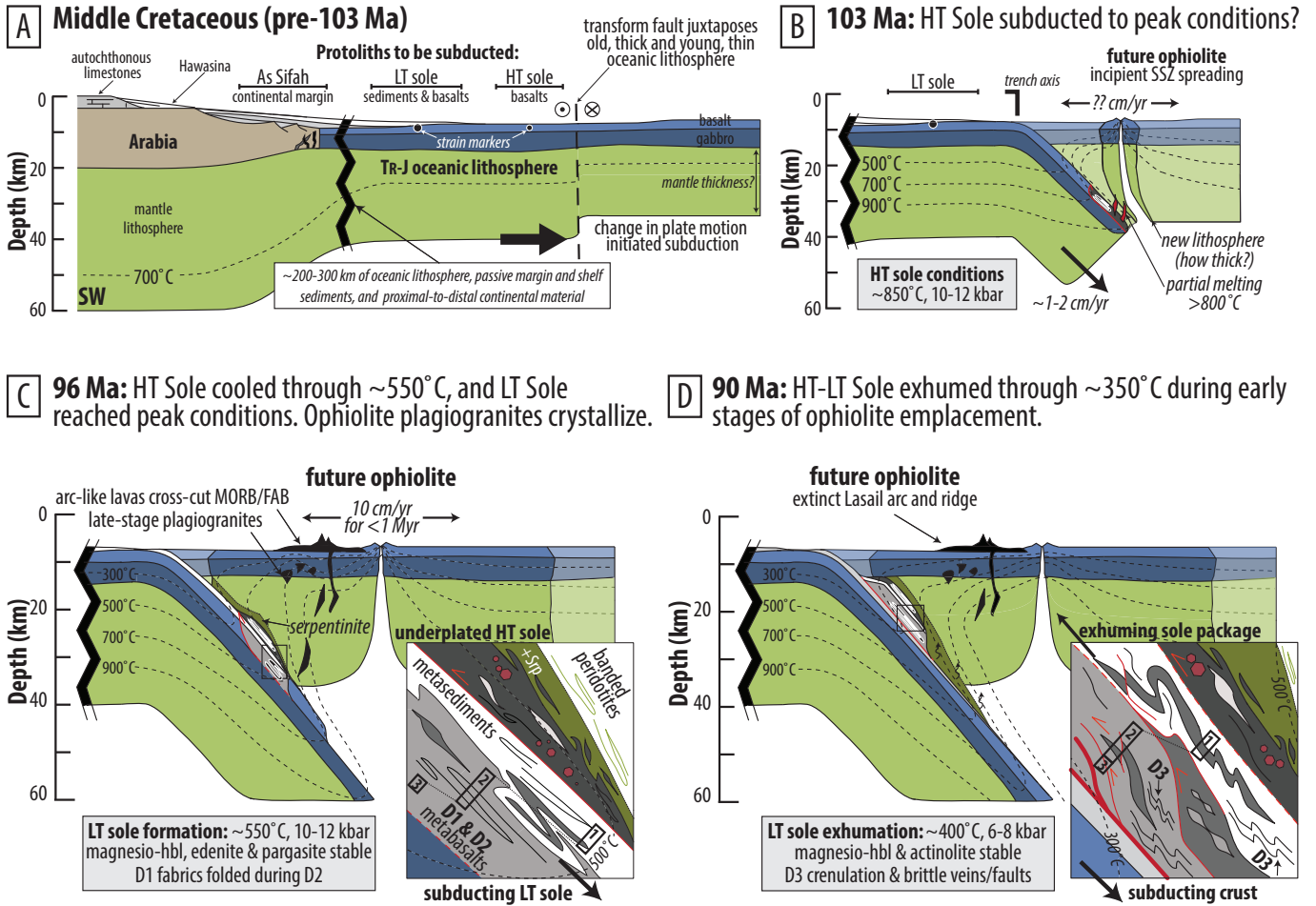


Figure 10: Schematic tectonic reconstruction illustrating the formation of the metamorphic sole. Compare time stamps with events highlighted in Figure 11. (A) Pre-subduction configuration. Black circles outlined in white are schematic strain markers. (B) HT sole formation at ~103 Ma. Incipient supra-subduction zone (SSZ) spreading created forearc basalt (FAB) or mid-ocean ridge basalt (MORB) geochemical signatures. (C) The LT sole reached similar peak depths as the HT sole, but tracked a cooler depth-temperature trajectory, and reached peak conditions at ~95-96 Ma. Inset shows isoclinal folding characteristic of the metamorphic sole, the ductile welding of the HT sole to the overriding ophiolite mantle, and the tectonic juxtaposition of the underplated HT-LT sole units. Black boxes labeled 1-3 and connected by dashed lines correspond to Sections 1-3 as observed in the BT-1B core. During subduction, each section might have experienced slightly different peak P-T, as inferred from the weak inverted metamorphic gradient with depth in the core. (D) The complete HT-LT sole package, constructed by progressive subduction, tectonic ‘slicing,’ and underplating, exhumed via return flow. Ductile shearing will eventually juxtapose Section 1 with Sections 2-3 during exhumation. Strain localized towards the bottom of the package in the LT sole under greenschist facies ductile-to-brittle conditions.

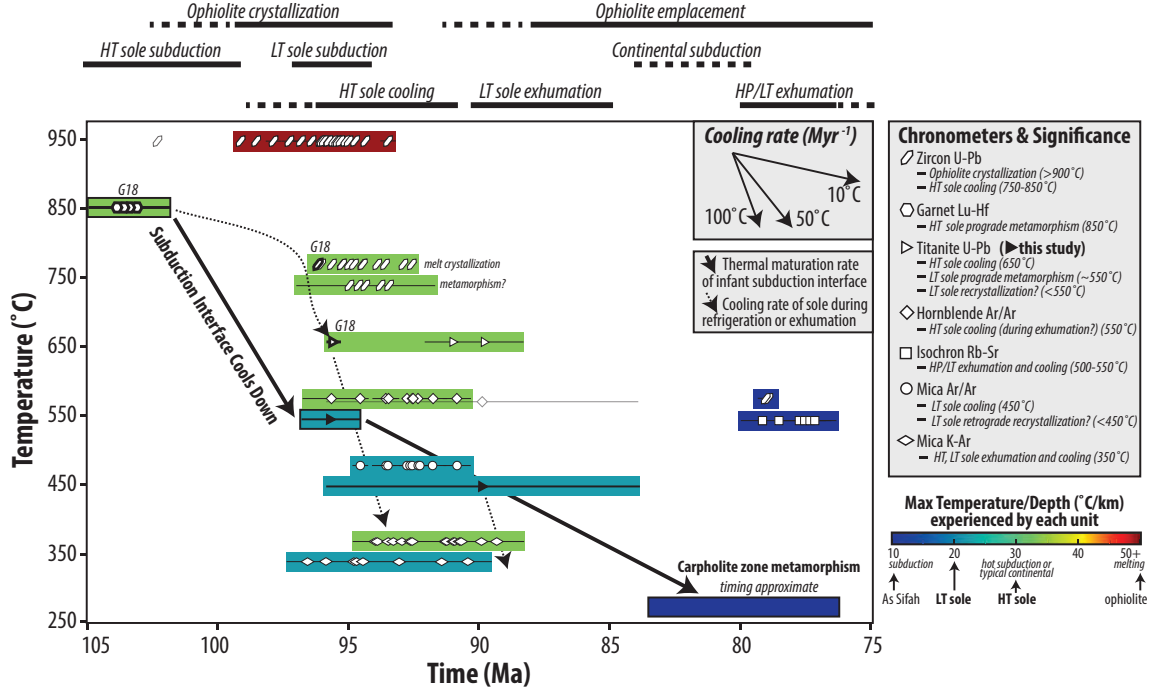


Figure 11: Temperature-time and tectonic evolution of the Samail ophiolite and metamorphic sole. Bold symbols labeled ‘G18’ are from Guilmette et al. (2018) for HT sole rocks from Wadi Tayin and Wadi Sumeini. Filled black symbols are new data presented in this study. Colored bars correspond to the maximum temperature-depth ratios characteristic of distinct tectonic sub-units, e.g. ophiolite crystallization (red), and progressive subduction of the HT sole (green), followed by LT sole (teal), and finally the Arabian continental margin (dark blue), illustrating interface cooling through time. Data outlined in black are timing and temperature conditions of prograde-to-peak subduction of the HT (green) and LT (teal) slivers. Data that are not outlined record cooling of each unit. Thick black arrows track refrigeration rates of the subduction interface.

96 Ma, which temporally overlaps with zircon crystallization in HT sole leucocratic lenses, and with plagiogranite crystallization in the ophiolite (Figs. 10, 11). Together these data provide new constraints on rates of rapid interface refrigeration (quantified below) over the first ~10 Myr of this subduction zone’s lifetime, which occurred in proximity to a forearc spreading center. Moreover, we believe that juxtaposition of this section of LT sole with the base of the HT sole was probably concurrent with exhumation of these rocks from depths of ~15 km accommodated by brittle structures (e.g., Searle & Cox, 1999, 2002; Agard et al., 2016; Soret et al., 2017). The initial exhumation of these rocks from maximum depths of 30 km implies ~15 km of return flow along the interface assuming a ~15-20 km thickness of the ophiolite before erosional denudation; otherwise, extensional thinning of the ophiolite above these metamorphic rocks was >50%.

In the broader framework of subduction infancy, the earliest episode of deformation and metamorphism is recorded in the HT sole. HT sole protoliths were dominantly basaltic and probably reflect subduction of distal seafloor with limited sediment cover, far from the Arabian continental margin (cf. Soret et al., 2017) (Fig. 10A). An alternative is that most incoming sediment was scraped off at shallower depths during initial convergence. The HT sole subducted to peak P-T conditions of $\sim 10\text{--}14$ kbar ($\sim 35\text{--}45$ km) and $\sim 750\text{--}850^\circ\text{C}$, consistent with a temperature-depth trajectory of $\sim 20\text{--}30^\circ\text{C/km}$ (Cowan et al., 2014; Searle et al., 2015; Soret et al., 2017). According to Lu-Hf dating of three samples from two locations reported by Guilmette et al. (2018), garnet growth and peak temperatures in the HT sole might have occurred as early as $\sim 103\text{--}104$ Ma (Fig. 9, 10B; 11), which predates igneous crystallization of the ophiolite plagiogranites at $\sim 96\text{--}95$ Ma by $\sim 6\text{--}8$ Myr. Moreover, the HT sole records cooling from near-peak T through $\sim 750^\circ$, 650° and 550°C captured by zircon U-Pb crystallization ages in the HT sole leucosomes (Warren et al., 2005; Styles et al., 2006; Rioux et al., 2016; Roberts et al., 2016), titanite U-Pb cooling ages (Searle et al., 2015; Guilmette et al., 2018), and hornblende $^{40}\text{Ar}/^{39}\text{Ar}$ cooling ages (Hacker, 1994) respectively (Fig. 11). Hornblende $^{40}\text{Ar}/^{39}\text{Ar}$ plateau ages of ~ 94 Ma and K-Ar ages for muscovite of ~ 92 Ma are only slightly younger than the plagiogranites (Hacker et al., 1996). Assuming Ar closure temperatures of $\sim 550^\circ\text{C}$ and $\sim 400^\circ\text{C}$ for hornblende and white mica, respectively, the HT sole records cooling rates of $\sim 75^\circ\text{C/Myr}$ between 95–92 Ma (Fig. 11).

If the ~ 103 Ma garnet ages from Guilmette et al. (2018) are reliable, then initial cooling near the new plate interface from $\sim 850^\circ\text{C}$ to $\sim 750^\circ\text{C}$ appears to have been significantly slower, proceeding at rates of only $\sim 10\text{--}20^\circ\text{C/Myr}$ (Fig. 11). This would suggest that initial underthrusting was very slow. Abundant geochronologic evidence demonstrates that this potential stage of early thrusting predates formation of the crustal section of the ophiolite, with the exception of two U-Pb zircon plagiogranite ages of 112 Ma and 102 Ma from Rioux et al. (2012), deemed ‘gabbroic pegmatite outliers.’ Rare diabase dikes intrude the metamorphic sole and tectonized harzburgite at the base of the ophiolite (Gregory, 1984). One such dike from the Hammah window, which truncates the HT foliation of the sole, but shares a static greenschist facies overprint with the sole, yielded a hornblende $^{40}\text{Ar}/^{39}\text{Ar}$ age of 93.7 ± 0.8 Ma (Hacker et al., 1996). This age has been interpreted as cooling of the dike (and the sole that it cuts) below $\sim 550^\circ\text{C}$ and the end of penetrative strain in the HT sole. The geometrical conundrum of mafic magma ascending to form the ~ 6 km thick

crustal section and locally cross-cutting the sole, while the HT sole was stored at depths of ~ 30 km, but rapidly cooling, is perplexing.

Whether the Lu-Hf ages for the HT sole garnets are confirmed regionally, it is readily apparent that the infant subduction zone environment cooled substantially during its first few million years of existence. Hornblende cooling ages in the HT sole and the new titanite crystallization ages in the LT sole in the BT-1B core indicate both units experienced temperatures of $\sim 550^\circ\text{C}$ contemporaneously (Fig. 11). Muscovite $^{40}\text{Ar}/^{39}\text{Ar}$ and K-Ar ages indicate rapid cooling of both HT and LT sole sections through 350°C between ~ 95 - 89 (Gnos & Peters, 1992; Hacker, 1994; Hacker & Mosenfelder, 1996) (Fig. 10D). Therefore, from ~ 96 to ~ 89 Ma, the HT sole rocks cooled from $\sim 750^\circ\text{C}$ to 350°C , and LT sole rocks cooled from $\sim 550^\circ\text{C}$ to 350°C , at a rate of ~ 55 - $100^\circ\text{C}/\text{Myr}$. These rapid cooling rates indicate continuous fast subduction at speeds > 5 cm/yr at these times.

Progressive cooling of the rocks along the interface is further supported by our new petrologic and geochronologic data that demonstrate the LT sole sequence reached peak P-T conditions of ~ 8 - 12 kbar (~ 30 - 40 km) and 550°C at ~ 95 - 96 Ma (Fig. 10C, 11), consistent with a depth-temperature trajectory of $\sim 15^\circ\text{C}/\text{km}$ (compare with $\sim 25^\circ\text{C}/\text{km}$ at 103 Ma; Fig. 9). This cooling appears to have occurred concurrently with changing physical properties of the interface, since the protoliths for the LT sole were different than those for the HT sole. The LT sole comprises dominantly sedimentary lithologies and basalts, which could reflect increasing sediment input with proximity to the continental margin (Fig. 10A).

Ductile strain during dynamic epidote-amphibolite facies metamorphism pervasively sheared the mafic and sedimentary layers forming the LT sole. We emphasize that the phyllites and amphibolites experienced unquantified, but very large, magnitudes of shearing. Hacker and Mosenfelder (1996) and Bucher (1991) arrived at similar P-T estimates for the LT sole rocks at Wadi Tayin and Asimah. These studies documented deformation under epidote-amphibolite facies metamorphic conditions followed by a greenschist facies overprint. However, their peak P was poorly quantified because the higher-P history is commonly only preserved in interiors of sub-mm sized, zoned amphibole porphyroblasts. Dynamic metamorphism continued into the greenschist facies until ~ 90 Ma and overprinted much of the evidence for the earlier higher-P deformation phase (Figs. 9; 10). The timing of exhumation-related deformation as recorded by our new titanite U-Pb ages is consistent with existing mica $^{40}\text{Ar}/^{39}\text{Ar}$ ages from phyllitic meta-cherts and calc silicates from nine

703 separate localities of the metamorphic sole, which yielded ages ranging from 90.0 to 93.6 \pm
 704 0.5 Ma (Hacker et al., 1996). While previously interpreted as cooling ages, it is also feasible
 705 that these ages record progressive recrystallization of white mica during exhumation-related
 706 ductile deformation.

707 Overlapping cooling ages indicate that both the HT and LT sole units were mechan-
 708 ically decoupled from the descending plate, by underplating or accretion, while fast sub-
 709 duction proceeded and the forearc block continued to refrigerate. Assuming a maximum
 710 ophiolite thickness of ~ 20 km, and considering that both the HT and LT soles each reached
 711 pressures equivalent to 30-40 km, then underplating/accretion must have been followed by
 712 upward movement of at least 10-20 km before juxtaposition with the base of the ophiolite.
 713 If the ophiolite was originally thicker, then removal of up to ~ 20 km of ophiolitic mantle
 714 must be explained to account for today's outcrop pattern (cf. Agard et al., 2020). An expla-
 715 nation that we favor is that the metamorphic sole units flowed upwards within a subduction
 716 channel shear zone (Cloos & Shreve, 1988a, 1988b). If the contact beneath the ophiolite
 717 dips at $\sim 25^\circ$, then the minimum up-dip return flow along the plate interface would be ~ 40
 718 km, and less if steeper (Fig. 10D).

719 It is important to emphasize that, because this young subduction zone was actively
 720 refrigerating, the fact that the HT and LT metamorphic soles experienced simultaneous
 721 cooling does not necessarily imply that these units were exhuming (i.e., decompressing) and
 722 flowing up the subduction channel shear zone. This inference is only possible by integrating
 723 geo-/thermochronology with structural petrology, which reveals fabric regeneration in LT
 724 sole rocks under lower P and T conditions at ~ 90 Ma (e.g. reduction of Si-in-phengite values,
 725 and actinolite overgrowths on hornblende; Fig. 5). Exhumation-related deformation appears
 726 to have been preferentially localized towards the structural base of the metamorphic sole
 727 package, imparting a pervasive greenschist facies overprint to wetter, weaker, finer-grained
 728 LT sole rocks, while structurally higher HT sole rocks largely escaped deformation and
 729 metamorphism during return flow (Fig. 10D).

730 Within the LT sole, metamorphism became increasingly static, and deformation in-
 731 creasingly brittle, as the rocks approached depths of ~ 15 -20 km during return flow (Figs.
 732 9; 10). The present contact between LT sole rocks and the ophiolite in the BT-1B core is a
 733 localized brittle fault zone. This fault contact may have originally been a thrust that juxta-
 734 posed different units in the subduction channel during syn-subduction exhumation, but we

interpret its most recent operation as a detachment fault at the base of the ophiolite that accommodated a later, brittle stage of exhumation of the metamorphic sole. Detachment faulting locally cut out the HT sole section.

7.2 Longer-term rates of hanging wall block refrigeration

Rapid cooling of the plate interface and leading edge of the overriding plate is expected where subduction of old, cold lithosphere is continuous and fast (Platt, 1975; Cloos, 1985; Hacker et al., 1996; Agard et al., 2020). Metamorphic studies have commonly proposed anti-clockwise P-T paths for subduction of HT sole rocks (Searle & Cox, 1999; Hacker, 1991), which reflects the initial refrigeration process, cooling rocks at a given depth through time. However, the LT sole appears to record a clockwise P-T trajectory, as indicated by chemical trends characterizing prograde-to-peak metamorphic amphibole zonations and by its record of both the subduction and exhumation segments of its P-T path (Fig. 9). The transition from an anti-clockwise to a clockwise P-T trajectory is a crucial hallmark of the interface refrigeration process as isotherms are deflected down along the interface, and may highlight different timescales of deep storage following underplating of distinct tectonic units.

In other ophiolite localities, sole metamorphism has been shown to culminate in blueschist facies conditions. For example, amphibolite facies meta-basalts in the Kiziltepe ophiolite in Turkey and the Newfoundland Appalachians record core-to-rim zonations from hornblende to glaucophane or crossite (Jamieson, 1977; Dilek & Whitney, 1997; Plunder et al., 2016). In Oman, blueschists and eclogites crop out SE of Muscat (Fig. 1) and reveal that continental margin subduction eventually reached P-T conditions of ~ 20 kbar and $\sim 500^\circ\text{C}$ (Wendt et al., 1993; Searle et al., 1994) at ~ 80 Ma (Warren et al., 2003). Therefore, the ~ 10 Myr window of rapid cooling after subduction initiation was followed by a period of more gradual cooling, on the order of $\sim 25\text{--}30^\circ\text{C}/\text{Myr}$ for another 15 Myr (Fig. 11), before this subduction zone eventually achieved a stable $\sim 7^\circ\text{C}/\text{km}$ thermal structure (Figs. 9, 11).

7.3 Significance of interface cooling and mechanical coupling for the ophiolite

Rapid changes in thermal structure during the first 10 Myr of subduction directly and dramatically influence the degree of mechanical coupling along the young interface. Progressive cooling leads to both changes in metamorphic mineral parageneses and the depths of prograde metamorphic dehydration of the shear zone (e.g., Poli & Schmidt, 1995; van Keken et al., 2011; Agard et al., 2016; Soret et al., 2019). Both of these phenomena strongly

impact the operative micro-physical deformation mechanisms. In general, the temporal progression in metamorphic rock stability from garnet-granulite, to garnet-amphibolite, to epidote-amphibolite at a given depth should lead to profound weakening. Compared to dry garnet- and pyroxene-bearing rocks, hydrous plagioclase-rich amphibolites are weak (Getsinger et al., 2013; Getsinger & Hirth, 2014) and may effectively localize strain during subduction infancy.

Numerical models show how rheological weakening along the interface can control upper plate stress state and may reduce mechanical coupling to a point where upper plate extension may occur (e.g. Lallemand et al., 2005; Androvičová et al., 2013; Čížková & Bina, 2013). In Oman, HT sole cooling, LT sole peak metamorphism, and ophiolite formation appear to have occurred concurrently (Figs. 10C, 11). This implies that the ophiolite was either young and hot when underthrusting began, or it formed soon after underthrusting began as strain progressively localized to greater depths at the plate-boundary scale. These observations may point to a fundamental feedback between interface cooling, mechanical weakening, and upper plate extension, leading to forearc spreading. Furthermore, the expected evolution in metamorphic and mechanical properties along the interface with interface cooling is consistent with documented trends in ophiolite lava chemistry. In the ophiolitic crust, there is a well-documented progression from MORB, to boninites, to calc-alkaline volcanics with stratigraphic height and time (Leng et al., 2012; Whattam & Stern, 2011; Stern et al., 2012). These geochemical changes may mirror evolving metamorphic characteristics of the interface, from hot and dry during HT sole subduction, to partially melted at peak HT sole conditions, to cooler and wetter during LT sole subduction.

8 Conclusions

Low-temperature metamorphic soles (LT soles) are high-strain subduction shear zones in tectonic contact with the base of large-slab ophiolites that contain vital information about rates of cooling, metamorphic conditions, and progressive strain localization during subduction infancy. Compared to their structurally higher, thinner, garnet-bearing, HT metamorphic soles counterparts, LT soles have been severely under-studied. One hundred and four continuous meters of LT sole were recovered during OmanDP drilling at Site BT-1B, in the footwall of the brittle Samail Thrust (i.e. Basal Fault). Following OmanDP core logging, we scrutinized the 104 m section with high sampling density (36 samples collected, 12 studied in detail) compared to the average field-based study using a combination of

structural, micro-structural, petrologic, and geochronologic techniques. The dense sample suite revealed a complex history of subduction- and exhumation-related deformation and metamorphism and allowed us to quantify interface cooling rates over the first ~ 10 Myr of this subduction zone's lifetime.

In this section of LT sole, upper phyllitic meta-sedimentary (34 m) and lower schistose meta-mafic rocks (70 m) record two stages of ductile deformation and metamorphism during subduction to epidote-amphibolite facies conditions (D_{1-2}). All lithologies were then variably overprinted by ductile greenschist facies retrogression (D_3) in a subduction channel configuration. We believe that tectonic juxtaposition of this section of LT sole with the HT sole involved ductile return flow that accommodated vertical translations of perhaps 10-20 km, thus bringing rocks from maximum depths of ~ 30 -40 km to the base of the overriding ophiolite mantle. Distributed, exhumation-related ductile strain evolved to localized brittle chloritized microthrust faulting, followed by calcite-filled normal-sense microfaulting, consistent with kinematic changes associated with exhumation and extensional denudation of the ophiolite.

Amphibole mineral zonations and Si-in-phengite values evolve systematically with progressive fabric development and constrain changes in P and T during subduction and return flow. The relative timing of deformation inferred from cross-cutting fabrics is consistent with absolute timing constrained by U-Pb ages of syn-kinematic titanite growth. Prograde-to-peak fabrics record mineral chemistry that indicates the LT sole reached peak P-T conditions of ~ 8 -12 kbar and ~ 450 -550°C. Titanite U-Pb ages constrain the timing of peak fabric development to ~ 95 -96 Ma. Dynamic greenschist overprinting occurred as P and T decreased and became progressively less pervasive by ~ 90 Ma. The timing of peak LT sole deformation and metamorphism post-dates recent garnet Lu-Hf crystallization ages in the HT sole by ~ 6 -8 Myr, overlaps with zircon U-Pb ages from crystallized partial melt lenses in the HT sole, and overlaps with plagiogranite crystallization in the ophiolite crust.

Our new petrologic and geochronologic data from detailed study of the 104 m LT metamorphic sole section sampled in the BT-1B drill core show that these rocks reached similar peak pressures (i.e. depths) as the structurally higher, garnet-bearing, HT metamorphic sole found elsewhere in Oman, but experienced $\sim 300^\circ\text{C}$ colder peak temperatures, and subducted later. These data support a revised tectonic model of progressive subduction, punctuated underplating, and return flow of the metamorphic sole beneath the Samail

Ophiolite while the infant interface was refrigerating. All of these dynamic processes occurred during subduction infancy, prior to ophiolite emplacement on the Arabian continental margin. Subduction infancy was characterized by rapid interface cooling, at rates of ~ 50 - $100^{\circ}\text{C}/\text{Myr}$ for ~ 8 - 10 Myr (with fastest cooling occurring over shorter time intervals within this window), followed by more gradual cooling of $\sim 25^{\circ}\text{C}/\text{Myr}$ for another 15 Myr, as the subduction zone evolved towards its characteristic steady-state thermal structure. This study affirms that low-temperature metamorphic sole rocks record crucial details regarding the first few million years of a subduction zone's lifetime, warranting fresh investigation of fine-grained LT sole rocks beneath other large-slab ophiolites around the world.

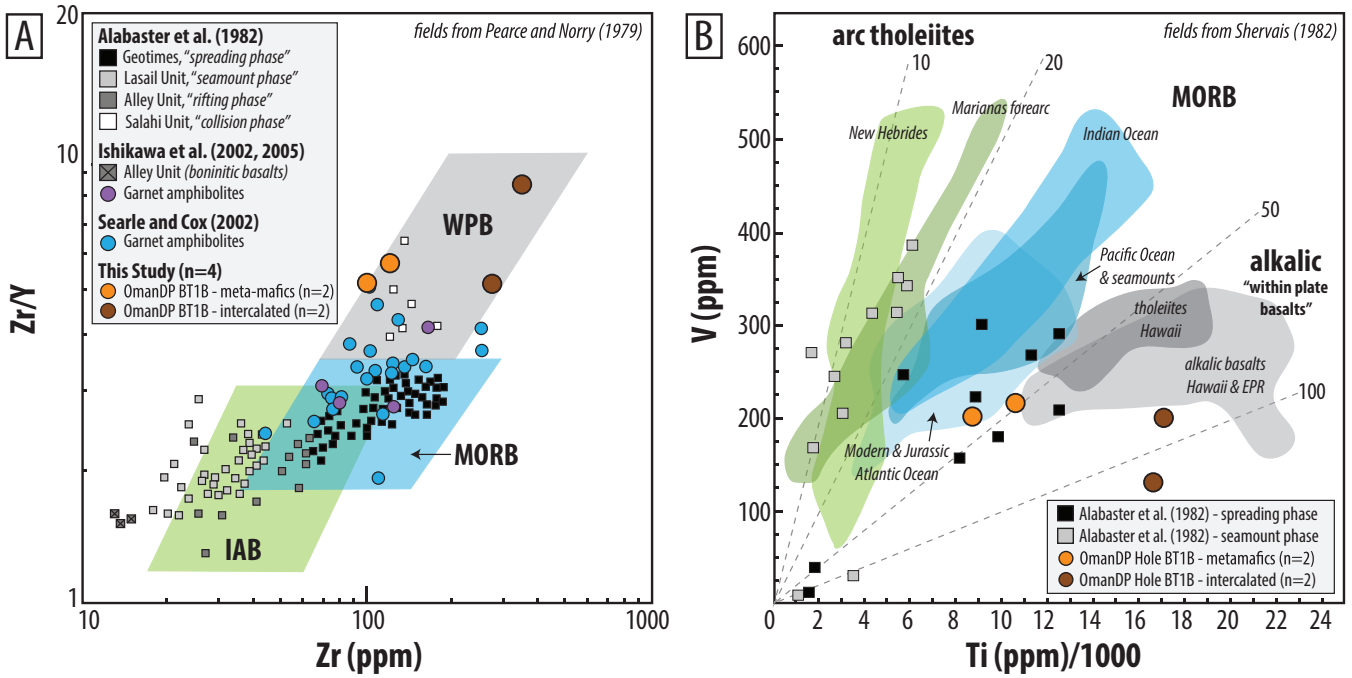


Figure A1: Bulk rock geochemistry from BT-1B core samples in orange and brown circles, compared to published values for ophiolite crust and the HT metamorphic sole. (A) Zr vs. Zr/Y discrimination diagram, following Pearce and Norry (1979). WPB = within-plate basalts, MORB = mid-ocean ridge basalts, IAB = island-arc basalts. (B) Ti vs. V discrimination diagram after Shervais (1982). Colored polygons encompass published geochemical data for lavas from various tectonic settings and geographic locations as indicated.

Appendix A Bulk Geochemistry and Metamorphic Mineralogy

A1 Bulk rock geochemistry

Bulk geochemistry for one meta-sediment, one intercalated meta-sedimentary and meta-mafic, and three meta-mafic samples was obtained. Samples were processed by Franklin & Marshall College lab manager Dr. Stanley Mertzmann. Homogeneous ~5-8 g samples (as best as possible considering limitations of sample size) were selected from shipboard quarter cores for analysis. Details of the laboratory procedure are summarized briefly herein.

Analyses were done using the Panalytical PW 2404 X-Ray Fluorescence spectrometer at Franklin & Marshall College. Total volatiles were first determined by placing the sample in a muffle furnace at 950°C for 1.5 hours, desiccating the sample, and comparing pre- and post-dessication weights. Anhydrous sample powders were then mixed with lithium tetraborate, transferred to a platinum crucible, heated until molten, and quenched to produce a glass disk for major element (SiO₂, TiO₂, Al₂O₃, Fe₂O₃ (total), MnO, MgO, CaO, Na₂O, K₂O,

Sample ID	AK199	AK209	AK222	AK264	AK295
Lithology	<i>metasediment</i>	<i>intercalated</i>	<i>intercalated</i>	<i>metamafic</i>	<i>metamafic</i>
SiO ₂	59.91	48.27	50.42	47.31	46.58
TiO ₂	2.13	2.87	2.77	1.76	1.45
Al ₂ O ₃	14.26	17.51	16.53	17.71	16.64
Fe ₂ O ₃ T	10.41	14.52	13.14	12.51	11.99
MnO	0.10	0.17	0.21	0.17	0.18
MgO	1.72	2.22	4.32	3.64	7.48
CaO	3.18	4.29	5.58	12.80	12.07
Na ₂ O	5.03	1.83	3.33	3.35	2.40
K ₂ O	1.91	6.38	2.80	0.63	0.47
P ₂ O ₅	1.12	1.53	0.78	0.29	0.17
Total	99.77	99.59	99.88	100.17	99.43
LOI	2.46	3.14	3.50	2.20	3.44
FeO	2.93	2.45	7.22	4.37	6.69
Fe ₂ O ₃	7.15	11.80	5.12	7.65	4.56
Rb	39.7	109.1	51.8	10.3	8.0
Sr	169	157	306	346	468
Y	40.4	63.0	41.3	21.1	19.2
Zr	270	315	351	120	99
V	121	202	129	214	199
Ni	29	48	19	64	130
Cr	22	11	8	194	307
Nb	42.8	52.0	53.1	16.7	13.1
Ga	15.0	25.3	23.8	19.0	18.0
Cu	12	13	19	132	59
Zn	95	168	128	98	86
Co	19	30	28	48	49
Ba	224	682	386	86	103
La	46	68	51	13	6
Ce	88	124	113	29	23
U	<1	<1	<1	<1	<1
Th	4.5	4.4	5.6	<1	1.1
Sc	14	24	21	32	33
Pb	1	1	4	3	2

Table A1: Major and trace element geochemistry for 1 meta-sedimentary (AK199), 2 intercalated (AK209, AK222), and 2 meta-mafic samples (AK264, AK295). ‘Intercalated’ samples contain both mafic and sedimentary material. Trace element concentrations are reported in ppm.

P₂O₅) XRF analysis. Ferrous Fe was determined using a modified Reichen et al. (1962) method. Trace element analysis was accomplished by mixing powders with a copolywax powder and pressing the mixture into a briquette (reported in ppm for Rb, Sr, Y, Zr, V, Ni, Cr, Nb, Ga, Cu, Zn, Co, Ba, U, Th, La, Ce, Sc, and Pb). Working curves for each element are determined by analyzing geochemical standards prepared as above; data have been synthesized by Abbey (1983) and Govindaraju (1994).

A2 X-Ray Diffraction

XRD was performed on the Bruker D8 Advance X-Ray Diffractometer in the Department of Geological Sciences at the University of Texas at Austin. Following visual

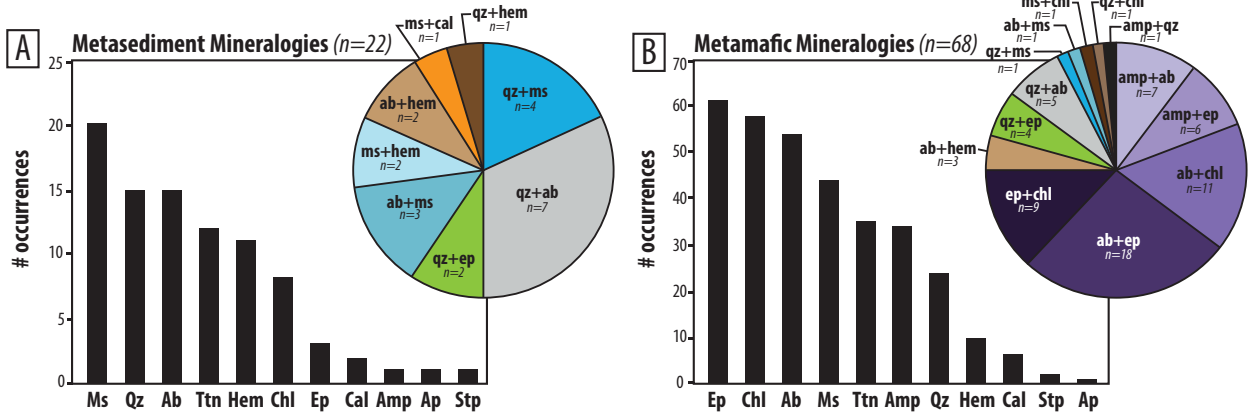


Figure A2: Results from XRD analyses of micro-drilled compositional layers for metasediments (A), and meta-mafics (B). All visually distinct layers were sampled in order to characterize petrologic variability. Results for each individual micro-drilled sample are shown in Supplementary Table A3. In (A-B), “n” indicates the number of samples analyzed. Pie charts show the number of occurrences of specified mineral pairs, representing the two most abundant phases in the sample, estimated from the relative intensities of X-Ray peaks.

characterization (and complemented by optical petrography of corresponding thin sections, described below) of shipboard quarter core samples, all visually distinct metamorphic layers and veins were micro-drilled into a powder using a fixed diamond-tipped drill. The powder was transferred to a mortar and pestle and ground to uniform fineness. Samples were placed on circular glass XRD mounts. Powdered samples were suspended in one drop of acetone and spread along the surface to produce a coat of even-thickness along the glass slide.

XRD patterns were collected for 142 micro-drilled layers and veins (68 meta-mafic layers, 22 meta-sedimentary layers, 49 veins of variable orientation with respect to the foliation, and 3 listervites). Samples were analyzed through a 2θ values of 4-65°. Patterns were stripped of background counts, refined with Fourier smoothing, and adjusted for x-offset where necessary using the Bruker EVA software. Identification of phases was accomplished using the ICDD PDF-2 Minerals database. Peaks were labeled for minerals that were properly identified and, where possible, confirmed petrographically.

XRD sample preparation and analysis was performed by undergraduate student Eytan Bos Orent, under supervision of Kotowski and Cloos.

MINERAL ASSEMBLAGES								
Sample ID	lithology	quartz	albite	muscovite	epidote	chlorite	mg-hbl	edenite
1 AK-80Z-01-199.25	metasediment	x	x	x	x	r, v, p		
2 AK-82Z-01-201.26	metasediment	x	x	x	x, a	r		
3 AK-86Z-04-209.35	metasediment	x, v	x	x	x, a	r		
4 AK-90Z-01-219.45	intercalated	x	x, r	x	x	x, r, v		x, c
5 AK-92Z-01-222.55	intercalated	x	x	x	x, a	x, r, v		x, c
6 AK-99Z-04-243.35	metamafic	x, v, p	x, r, p		x, v	x, r, v		x
7 AK-103Z-02-253.7	metamafic	v, p	p, r		x, a	r, p, v	o	x, c
8 AK-106Z-03-264	metamafic	v	x, p	m	x, a, v	v, p, r		x
9 AK-109Z-02-268.85	metamafic	v	x	m	x	x, v, p, r	x	o
10 AK-111Z-02-275.35	metamafic	v	x, v, p, ps	ps	x, a, ps	v, p, r	x, o, c	x, c
11 AK-112Z-02-278.5	metamafic	v	x, p, ps	ps, m	x, ps	p, r		x
12 AK-125Z-01-295.95	metamafic		x, p		x	x, o, ps	x, c	

		pargasite	actinolite	apatite	titanite	Fe-Ti-O	calcite	other
1 AK-80Z-01-199.25	metasediment			x		x, b		
2 AK-82Z-01-201.26	metasediment			x	x	x, b		
3 AK-86Z-04-209.35	metasediment			x	x	x, b		tur, m
4 AK-90Z-01-219.45	intercalated	x, c	o	m		b	v	
5 AK-92Z-01-222.55	intercalated	x, c				x, b	v	
6 AK-99Z-04-243.35	metamafic	o				x, v	v	
7 AK-103Z-02-253.7	metamafic	o	o			x, b	v	
8 AK-106Z-03-264	metamafic		o			x, b		
9 AK-109Z-02-268.85	metamafic		x			x	p, v	
10 AK-111Z-02-275.35	metamafic		o				v	
11 AK-112Z-02-278.5	metamafic	x				b	v	sulfides
12 AK-125Z-01-295.95	metamafic		x, c				v	sulfides

x = present, foliation-forming	c = cross-cuts foliation
v = vein	p = patchy
b = porphyroblasts	a = allanite cores of epidotes
o = rims & overgrowths	m = minor, $\leq 5\%$
r = replacement	ps = mineral occurs as pseudomorph?

Table A2: Parageneses of samples selected for detailed EMPA and microstructural analyses. Sample IDs are listed in the left column, and are read as follows: AK-*core*Z-*section*-*depth* *downhole* (*m*).

Appendix B Shipboard Core Logging Methods

BT-1B was visually and instrumentally described according to Integrated Ocean Drilling Project (IODP) protocols on board the Japanese drillship Chikyu in August-September 2017. This particular contribution focuses on post-Chikyu structural and petrologic characterization in the lowermost 100 m of the BT-1B core.

Onboard Chikyu, we characterized host rock lithology, taking note of colors and mineralogy, as well as distributions and types of veins cutting the host rock. Vein descriptions included mineralogy and modal proportions, grain size, thickness, and morphology. Host rock structure, which is summarized briefly in Section 3, was described as massive, brecciated, cataclastic, “fragmented by veins” (i.e. contains brecciated veins), or foliated; localized structures were described as faults (mm-to-10’s of cm scale), cataclasites (mm-to-cm scale), single veins and/or vein sets (and mineralogy), shear zones (mm-to-cm scale), folds, and cracks (i.e. did not contain mineralization or apparent displacement; only documented

[t]

Sample	Thin Section Notes	XRD Results	Petrographically Confirmed	Mystery Peaks
Muscovite				
AK-80Z-01-199.23a	plage, stlp?, tm, ilm	albite, muscovite, amphibole, titanite, chlorite	albite, muscovite, hematite, chlorite	
AK-80Z-01-199.23b	an, stlpnomelane?, wm	albite, quartz, hematite, titanite, muscovite, chlorite	albite, quartz, muscovite, hematite, chlorite, titanite	
AK-80Z-01-199.23c		quartz, albite	quartz, albite	
AK-80Z-01-199.23d		quartz, albite, titanite, muscovite, chlorite	quartz, albite, muscovite, chlorite, titanite	
AK-80Z-01-199.25e		quartz, albite, titanite, chlorite, phlogopite	quartz, albite, muscovite	
AK-81Z-01-200.2a		quartz, hematite, albite, muscovite, titanite, apatite	quartz, hematite, muscovite, titanite	
AK-82Z-01-201.26b		muscovite, hematite, titanite	muscovite, hematite	
AK-82Z-01-201.26c		quartz, muscovite, stlpnomelane, apatite, albite, chlorite, titanite	quartz, muscovite, chlorite, stlpnomelane, apatite	34.8, 35.4
AK-82Z-01-201.5a		quartz, albite, stlpnomelane, muscovite	quartz, albite, muscovite	
AK-82Z-01-201.5b		albite, quartz, stlpnomelane, titanite, muscovite	albite, quartz, muscovite	
AK-82Z-01-201.5c		albite, hematite, phlogopite, titanite, chlorite	albite, hematite	
AK-82Z-02-201.65b		quartz, hematite, albite, muscovite, titanite	albite, hematite, muscovite, quartz, titanite	
AK-82Z-02-201.65c		muscovite, albite, titanite, hematite,	muscovite, albite, titanite, hematite, chlorite	19.7, 34.8
AK-82Z-03-202.9a		albite, calcite, muscovite, titanite, apatite	albite, muscovite, titanite, calcite	
AK-82Z-03-202.9b		calcite, albite, muscovite, titanite, hematite	muscovite, calcite, albite, hematite	
AK-82Z-03-202.9c		hematite, muscovite, titanite	hematite, muscovite, titanite	20.5
AK-86Z-01-207b		quartz, epidote, phlogopite, chlorite, titanite	quartz, muscovite, chlorite, epidote	
AK-86Z-01-207c		quartz, epidote, phlogopite, titanite, chlorite	quartz, epidote, muscovite, titanite	
AK-86Z-01-207d		quartz, epidote, amphibole, phlogopite, chlorite, albite, titanite	quartz, epidote, muscovite, albite, chlorite, titanite, amphibole	
AK-86Z-04-209.3b	wm, oxide, tm, ep, an, ab, chl	quartz, muscovite, titanite, amphibole	quartz, muscovite, titanite	27.5
AK-86Z-04-209.3c	standard metasediment	quartz, albite, muscovite, hematite, titanite, chlorite	quartz, muscovite, albite, chlorite, titanite, hematite	
AK-86Z-04-209.3d	standard metasediment	albite, quartz, amphibole, titanite, muscovite	albite, quartz, hematite, muscovite, titanite	
AK-86Z-04-209.1b		albite, hematite, calcite	albite, hematite, calcite	
AK-86Z-04-209.1c		albite, amphibole, titanite, phlogopite, chlorite	albite, hematite, chlorite, muscovite	
AK-90Z-01-219.45a		quartz, albite, epidote, titanite, chlorite, phlogopite	quartz, albite, epidote, chlorite	
AK-90Z-01-219.45b		albite, chlorite, epidote, amphibole, titanite	albite, chlorite, amphibole, epidote	
AK-90Z-01-219.45c		quartz, albite, epidote, amphibole, stlpnomelane, chlorite, titanite	quartz, albite, amphibole, epidote, stlpnomelane	
AK-92Z-01-222.53b	typical metamafic (intercalated lens)	amphibole, epidote, quartz, muscovite, apatite	amphibole, epidote, quartz, muscovite (not in TS)	23.5
AK-92Z-01-222.53c		amphibole, albite, chlorite, muscovite, epidote, titanite	amphibole, albite, epidote, chlorite, muscovite	
AK-92Z-01-222.55d		albite, chlorite, muscovite, epidote, titanite	albite, chlorite, epidote, muscovite	
Metamafics				
AK-96Z-02-232.45c		epidote, albite, titanite, chlorite, muscovite	epidote, albite, chlorite, muscovite, titanite	
AK-96Z-04-234.2c		quartz, albite, amphibole, muscovite, titanite, epidote, chlorite	quartz, amphibole, albite, muscovite	
AK-96Z-04-234.2e		titanite, chlorite, muscovite, albite, epidote, amphibole	albite, chlorite, epidote, muscovite, quartz, titanite	
AK-96Z-04-234.2f		albite, titanite, epidote, apatite, muscovite, phlogopite, amphibole	albite, epidote, muscovite, apatite, titanite	
AK-97Z-01-234.9b		quartz, hematite, albite, muscovite, titanite, chlorite	quartz, muscovite, titanite, hematite	
AK-97Z-01-234.9c		quartz, epidote, titanite, muscovite, chlorite, calcite, albite	quartz, chlorite, muscovite, albite, epidote, titanite	33
AK-97Z-03-236.59b		epidote, quartz, phlogopite, albite, titanite, chlorite	epidote, quartz, albite, chlorite, muscovite	
AK-97Z-03-236.59c	ab, qz, stlp, chl, ep, tm, pumpellyite, act	epidote, chlorite, nickel, titanite, calcite, diamond, quartz	epidote, chlorite, titanite, calcite	
AK-97Z-03-236.59d	qz, ab, ep, chl, zo, tm, ilm, amph	albite, amphibole, epidote, chlorite, hematite, quartz, titanite	albite, chlorite, epidote, hematite, quartz, muscovite	
AK-97Z-03-236.59e	ab, ep, chl, ilm? Hem?	chlorite, albite, quartz, amphibole, epidote	chlorite, albite, epidote, quartz	
AK-98Z-02-238.3a	typical metamafic	muscovite, hematite, titanite, chlorite, amphibole	muscovite, chlorite, hematite, albite	
AK-98Z-02-238.3b		albite, epidote, hematite, titanite, chlorite, amnrite	epidote, albite, chlorite, titanite, hematite, muscovite	25.6
AK-98Z-02-238.3c		epidote, chlorite, titanite, quartz	epidote, chlorite, albite, titanite, quartz	33
AK-98Z-02-238.7c		albite, quartz, chlorite, titanite, epidote	albite, chlorite, epidote, quartz, muscovite	
AK-98Z-04-240b		quartz, albite, epidote, hematite, titanite, chlorite, phlogopite, calcite	albite, quartz, epidote, chlorite, hematite, muscovite	
AK-98Z-04-240c		epidote, quartz, chlorite, phlogopite, titanite	epidote, chlorite, quartz, titanite, muscovite	
AK-98Z-04-240d		epidote, chlorite, albite, titanite	epidote, chlorite, albite, titanite	
AK-99Z-03-242.1b		quartz, albite, epidote, chlorite, titanite, hematite, phlogopite	albite, chlorite, epidote, amphibole, muscovite	
AK-99Z-03-242.1c		albite, quartz, hematite, epidote, chlorite, titanite, muscovite	albite, chlorite, epidote, quartz, hematite, muscovite, amphibole, titanite	
AK-99Z-04-243.33a	typical metamafic	epidote, chlorite, titanite	epidote, chlorite, titanite, muscovite	27.2, 27.5
AK-99Z-04-243.33b	typical metamafic	quartz, albite, epidote, chlorite, titanite, hematite	quartz, albite, chlorite, titanite	26.2
AK-100Z-02-244.55c		quartz, epidote, titanite, chlorite	quartz, epidote, chlorite, titanite	30
AK-100Z-02-244.55d		epidote, quartz, muscovite, chlorite, titanite	epidote, chlorite, quartz, titanite, muscovite	
AK-102Z-01-250.25b		amphibole, albite, epidote, titanite, chlorite, muscovite	amphibole, albite, epidote, chlorite, titanite	
AK-102Z-01-250.25c		epidote, albite, titanite, amphibole, muscovite	epidote, albite, amphibole, chlorite, muscovite, titanite	
AK-103Z-02-253.7b		epidote, albite, muscovite, amphibole	albite, epidote, amphibole, muscovite, chlorite	
AK-106Z-03-264b	amph, ab, ep, chl, tm	epidote, albite, amphibole, titanite	amphibole, epidote, albite, titanite	
AK-108Z-02-265.8c	typical metamafic	albite, epidote, titanite, chlorite, phlogopite	albite, epidote, amphibole, muscovite, chlorite, titanite	

Table A3: All XRD analyses from visually distinct compositional layers, and foliation-parallel and cross-cutting veins.

[t]

AK-109Z-02-268.8c	typical metamafic	albite, epidote, amphibole, calcite, titanite, phlogopite	amphibole, albite, epidote, calcite, chlorite
AK-109Z-04-270.35a	qz, ep, ap	albite, epidote, titanite, muscovite, amphibole	albite, epidote, muscovite, amphibole
AK-109Z-04-270.35b	typical metamafic, blue amphiboles	epidote, quartz, albite, chlorite, amphibole, titanite	epidote, quartz, chlorite, amphibole, muscovite
AK-109Z-04-270.35c	typical metamafic, blue amphiboles	epidote, epidote, albite, phlogopite, chlorite	quartz, albite, chlorite, epidote, muscovite, stannomelane
AK-109Z-04-270.35d	typical metamafic, blue amphiboles	epidote, quartz, muscovite, titanite, albite, chlorite	epidote, quartz, chlorite, muscovite, titanite
AK-110Z-01-271.2a	typical metamafic, wm, qz	albite, epidote, muscovite, chlorite	albite, epidote, muscovite, chlorite
AK-110Z-01-271.2c	typical metamafic, wm, qz, pseudomorph of ???	epidote, calcite, chlorite, albite, quartz, titanite	epidote, albite, chlorite, amphibole, titanite, calcite, quartz
AK-110Z-03-273.05a	typical metamafic	epidote, chlorite, albite, titanite, amphibole	epidote, chlorite, amphibole, muscovite, titanite
AK-110Z-03-273.05b	typical metamafic	albite, epidote, titanite, chlorite, muscovite	albite, epidote, chlorite, amphibole, titanite
AK-110Z-03-273.05d	typical metamafic	epidote, chlorite, titanite	epidote, chlorite, amphibole, titanite
AK-111Z-01-274b	ep, qz	epidote, amphibole, titanite, albite, calcite	epidote, amphibole, chlorite, titanite
AK-111Z-01-274c	ep, cal, ab, amph	albite, epidote, calcite	albite, epidote, calcite, chlorite, amphibole, muscovite
AK-111Z-01-274d	similar to c	albite, epidote, calcite	albite, epidote, amphibole, calcite, chlorite, titanite
AK-111Z-01-274e	more amphibole	albite, epidote, amphibole, calcite, titanite	albite, epidote, amphibole, chlorite, muscovite, titanite
AK-111Z-02-275.35c	green schist standard assemblage, wm, ab	albite, epidote, chlorite, titanite	albite, chlorite, epidote, titanite
AK-111Z-02-275.35d	green schist standard assemblage, wm, ab	epidote, amphibole, albite, muscovite, chlorite, titanite	epidote, albite, amphibole, chlorite, muscovite, titanite
AK-111Z-03-276.05a	amph, ep, ab, chl, wm (musc)	albite, epidote, muscovite, chlorite, titanite (?)	albite, epidote, chlorite, muscovite
AK-111Z-03-276.05d	blue-green amphib, ep, chl	epidote, amphibole, albite, calcite, muscovite, chlorite	epidote, amphibole, albite, chlorite, muscovite
AK-112Z-02-278.5a	ep, chl, cel, qz, needlely crystal	albite, chlorite, epidote, titanite, muscovite	albite, chlorite, epidote, muscovite
AK-112Z-02-278.5c	similar to a but more amphibole	epidote, chlorite, calcite, titanite, amphibole	epidote, chlorite, amphibole, calcite, muscovite, titanite
AK-112Z-02-278.5d	similar to a but most amphibole (potentially sodic)	amphibole, quartz, epidote, albite	amphibole, epidote, quartz
AK-120Z-02-290.25a	lawsonite pseudomorphs? (combination of mica, epidote)	albite, epidote, amphibole, phlogopite	albite, epidote, amphibole, muscovite, chlorite
AK-120Z-02-290.25c	sulfide, green amphib, ab, chl	amphibole, albite, epidote, chlorite, titanite	amphibole, albite, epidote, chlorite, titanite
AK-121Z-02-291.5a	amph, chl, ab, ep	amphibole, albite, quartz	amphibole, albite, epidote, quartz, muscovite
AK-121Z-02-291.5b	amph, chl, ab, ep	albite, chlorite, amphibole, epidote	albite, chlorite, amphibole, epidote
AK-121Z-02-291.5c	amph, chl, ab, ep	albite, epidote, chlorite, muscovite	albite, epidote, muscovite, chlorite
AK-125Z-01-295.95a	blue-green amphib, ep, chl, oxide	amphibole, albite, epidote, chlorite, titanite	amphibole, epidote, chlorite, albite, titanite
AK-125Z-04-297.8b	amph, oxide, cel, ep, tm	amphibole, albite, chlorite, titanite	amphibole, albite, epidote, chlorite
AK-125Z-04-297.8c	similar to greenschist facies minerals from b	albite, amphibole, titanite, muscovite, chlorite	albite, hematite, muscovite, chlorite, titanite
AK-125Z-04-297.8d	similar to greenschist facies minerals from b	albite, muscovite, titanite, amphibole, chlorite	albite, muscovite, hematite, chlorite, epidote, titanite
AK-125Z-04-298b	act, qz, ab, chl, ep, blue-green amphib, sulfide	albite, amphibole, chlorite, epidote, phlogopite	albite, amphibole, chlorite, epidote, muscovite

AK-83Z-01-201.26a	oblique	albite, amphibole, epidote, titanite, chlorite	albite, epidote, amphibole, chlorite, titanite, muscovite
AK-83Z-01-201.26d	oblique	quartz, muscovite	quartz, muscovite
AK-83Z-02-201.65a	foliation parallel	albite, quartz, hematite, muscovite, titanite	albite, quartz
AK-83Z-03-202.9d	foliation parallel	calcite, muscovite	calcite, muscovite
AK-86Z-01-207a	foliation parallel	quartz, calcite	quartz, quartz
AK-86Z-04-209.1a	foliation parallel	calcite, quartz, hematite	calcite, quartz
AK-86Z-04-209.3a	foliation parallel, qz	quartz, muscovite, albite, titanite, amphibole	quartz, muscovite, albite
AK-92Z-01-222.53a	foliation parallel, typical metamafic	quartz, albite, epidote, muscovite, chlorite	quartz, albite, epidote, muscovite (not in TS), chlorite
AK-96Z-02-232.45a	foliation parallel	quartz, calcite	quartz, calcite
AK-96Z-02-232.45b	foliation parallel	quartz, epidote, chlorite	quartz, epidote, chlorite
AK-96Z-04-234.2a	foliation parallel	calcite, quartz, albite, amphibole, titanite	calcite, quartz
AK-96Z-04-234.2b	foliation parallel	albite, titanite, epidote, quartz, amphibole, chlorite	albite, epidote, amphibole, quartz
AK-96Z-04-234.2d	crosscutting	quartz	quartz
AK-97Z-01-234.9a	foliation parallel	quartz, calcite	calcite, quartz
AK-97Z-03-236.59a	foliation parallel, typical metamafic	calcite, nickel, quartz, diamond	calcite, quartz
AK-97Z-03-236.59f	foliation parallel, typical metamafic	calcite, quartz, albite, chlorite, biotite	calcite, quartz
AK-98Z-02-238.3c	foliation parallel	quartz, albite, epidote, chlorite	calcite, quartz, muscovite (wall rock), albite
AK-98Z-02-238.3d	foliation parallel	quartz, epidote, albite	quartz, albite
AK-98Z-02-238.3e	foliation parallel	quartz	quartz, albite, epidote
AK-98Z-02-238.7a	crosscutting	quartz, epidote, albite, chlorite, titanite, muscovite	quartz
AK-98Z-02-238.7b	crosscutting	quartz, stannomelane, chlorite, albite, epidote, titanite	quartz, albite, epidote, chlorite
AK-98Z-02-238.7d	crosscutting	quartz, chlorite, epidote	quartz, stannomelane, chlorite, epidote
AK-98Z-04-240a	foliation parallel	calcite, quartz, albite	calcite, quartz
AK-99Z-03-242.1a	foliation parallel	calcite, quartz, epidote, titanite, albite, chlorite	calcite, quartz, epidote
AK-99Z-03-242.1d	foliation parallel	quartz, albite, calcite, epidote, chlorite	calcite, quartz, calcite
AK-99Z-04-243.35c	foliation parallel, typical metamafic	quartz, albite, epidote, chlorite, titanite	quartz, epidote, calcite
AK-99Z-04-243.35d	foliation parallel, typical metamafic	quartz, nickel, diamond	quartz, chlorite, albite, epidote
AK-100Z-02-244.55a	brecciated	quartz	quartz
AK-100Z-02-244.55b	brecciated	epidote, quartz, muscovite, titanite, albite	epidote, quartz

Table A3: Continued.

[t]

AK-102Z-01-250.25a	crosscutting	calcite, chlorite	calcite, chlorite	calcite, chlorite
AK-103Z-02-253.7a	crosscutting	quartz, calcite	quartz, calcite	quartz, calcite
AK-103Z-02-253.7c	foliation parallel	epidote, calcite, amphibole	epidote, calcite, amphibole	epidote, calcite, amphibole
AK-106Z-03-264a	foliation parallel, typical metamafic	quartz, epidote, albite, amphibole	quartz, epidote, albite, amphibole	quartz, epidote (elongated habit)
AK-108Z-02-265.8a	foliation parallel, ep. typical metamafic	quartz, epidote, albite	quartz, epidote, albite	quartz, epidote
AK-108Z-02-265.8b	oblique, typical metamafic, mostly ep	quartz, epidote, albite	quartz, epidote, albite	quartz, albite, epidote
AK-109Z-02-268.8a	foliation parallel, cal, qz	calcite, phlogopite, albite	calcite, phlogopite, albite	calcite
AK-109Z-02-268.8b	foliation parallel, ep, typical metamafic	quartz, calcite, epidote	quartz, calcite, epidote	quartz, calcite, epidote
AK-110Z-01-271.2b	crosscutting, typical metamafic, ym, qz	calcite, epidote	calcite, epidote	calcite, epidote
AK-110Z-03-273.05c	foliation parallel, cal, qz, ampb, ab	quartz, calcite, albite, amphibole, muscovite	quartz, calcite, albite	quartz, calcite, albite
AK-111Z-01-274a	crosscutting, cal	calcite	calcite	calcite
AK-111Z-02-275.55a	foliation parallel, qz, cal	calcite, albite, chlorite	calcite, albite	calcite, albite
AK-111Z-02-275.55b	foliation parallel, ep, qz, cal	epidote, calcite, albite, amphibole, chlorite	epidote, calcite, albite, chlorite	epidote, calcite, albite, chlorite
AK-111Z-03-276.05b	foliation parallel, ep, chl, oxide, cal	albite, quartz, epidote, phlogopite	albite, quartz	albite, quartz
AK-111Z-03-276.05c	crosscutting, cal, qz, chl, ampb/ep aggregate	calcite	calcite	calcite
AK-112Z-02-278.5b	foliation parallel, ep	calcite	calcite	calcite
AK-120Z-02-290.25b	foliation parallel, ep, qz, mystery radiating mineral	epidote, albite	epidote, albite	epidote, albite
AK-125Z-04-297.8a	crosscutting, qz, ep	quartz, epidote, calcite, albite, muscovite	quartz, epidote, calcite	quartz, epidote, calcite
AK-125Z-04-298a	crosscutting, qz, cal, chl, ap	quartz, calcite	quartz, calcite	quartz, calcite
AK-125Z-04-298c	foliation parallel, ep, qz, chl	quartz, ankerite, muscovite	quartz, chlorite, epidote	quartz, chlorite, epidote

Table A3: Continued.

in listvenites). We documented cross-cutting relationships and relative ages of structural features, stable host-rock and vein mineralogy relative to deformation events, and the down-hole abundance and petrologic characteristics of brittle deformation features. Shipboard thin sections were made for first-pass petrologic and micro-structural descriptions.

After shipboard logging, we collected 36 samples from the 100 m of sub-ophiolite metamorphics for analysis at the University of Texas at Austin (8 phyllitic, mica-rich meta-sediments and 28 epidote- and amphibole-rich meta-volcanics). Samples were collected at roughly even intervals down-core and were selected to represent the core's lithological and structural heterogeneity. Features of special interest were also sampled. Each sample was cut into a microprobe polished 30 μm thin section, oriented parallel to lineation and perpendicular to foliation.

Appendix C Electron Microprobe techniques

C1 Qualitative X-Ray Mapping

Qualitative X-ray compositional maps were acquired on the JEOL JXA-8200 electron microprobe in the Department of Geological Sciences at the University of Texas at Austin. Polished 30 μm thin sections were analyzed using a 15 kV accelerating voltage, focused beam, 50-200 nA current, 1-6 μm step size, and 1 ms dwell time. X-ray maps for Si, Al, Ca, Mg, Fe, Na, K, Mn, Ti, and P were collected. Post-processing to produce false color compositional maps was done in ImageJ software by merging element channels with assigned colors.

C2 Quantitative Point Analyses

Quantitative analyses were collected for amphiboles and micas on the JEOL JXA-8200 electron microprobe in the Department of Geological Sciences at UT Austin. Polished 30 μm thin sections were analyzed using a 15 kV accelerating voltage, a focused (1 μm) beam (for all hydrous phases, due to extremely fine mica grain sizes), 10 nA current, and 30 s counting time for all elements. Synthetic compounds and natural homogeneous minerals were used as standards, and secondary standards were analyzed throughout analytical procedures. Data were processed using the JEOL ZAF procedure. Major element oxide weight percents were converted to cations per formula unit first by calculating water by difference, then assuming 24 and 12 atoms of O for amphibole and white mica, respectively (including H as a cation).

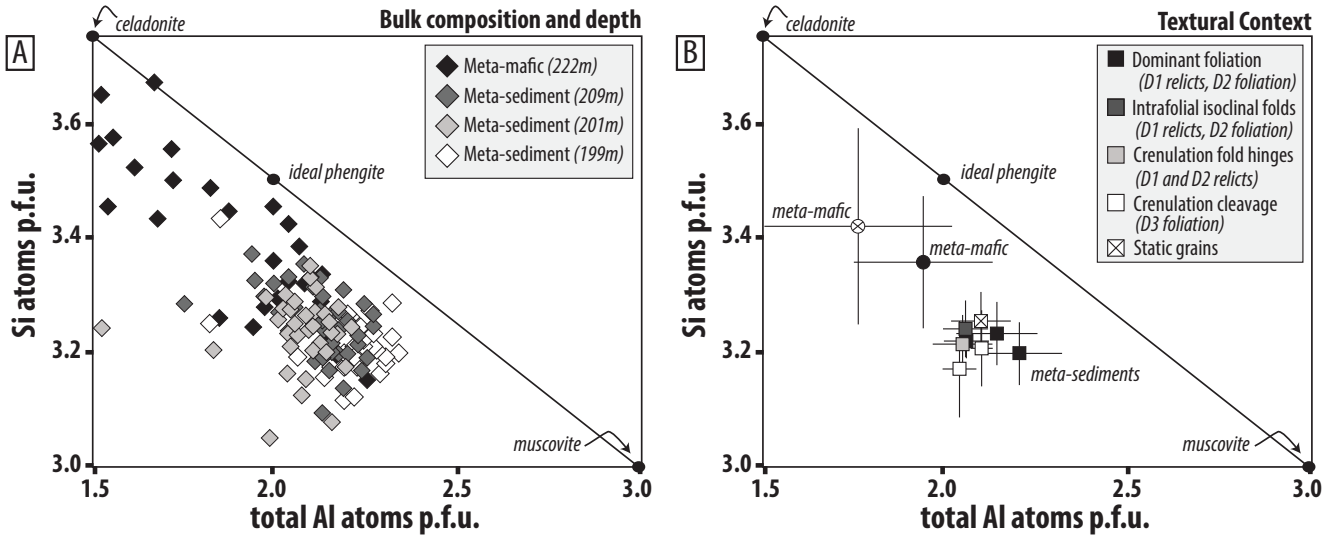


Figure C1: Mica chemistry for meta-sediments (199, 201, 209m) and a meta-mafic sample (222 m). (A) Total Al vs. Si atoms p.f.u. (B) Results grouped by micro-textural context. See text for discussion.

Amphibole calculations assigned the T-site a total of 8 cations ($\text{Si} + \text{Al}^{iv}$). Remaining Al was assigned to Al^{vi} . Fe^{2+} , Ca and Na were assigned to the M4 site for a total of 2 cations, and excess Na was assigned to the A site. Ferric and ferrous iron were calculated based on cation normalization to achieve charge balance. Nomenclature and classification was determined following recommendations approved by the Commission on New Minerals Nomenclature and Classification (CNMNC) of the International Mineralogical Association (IMA) (Hawthorne et al., 2012).

Texture	cores	rims	foliation	oblique	cores	rims	cores	mantles	rims	cores	rims	cores	rims	cores	rims	unzoned	cores	rims
Sample	AK219	AK219	AK222	AK222	AK243	AK243	AK253	AK253	AK253	AK264	AK264	AK268	AK268	AK275	AK275	AK278	AK295	AK295
#analyses	30	8	37	14	22	16	37	5	21	51	12	21	19	14	16	58	21	3
SiO ₂	43.19	53.56	43.39	43.32	46.08	44.41	45.05	43.09	53.84	45.56	55.49	51.76	46.44	45.60	52.85	44.45	53.04	48.16
TiO ₂	0.40	0.12	0.38	0.37	0.37	0.44	0.38	0.42	0.08	0.36	0.05	0.18	0.34	0.37	0.11	0.41	0.12	0.26
Al ₂ O ₃	13.96	2.74	14.35	14.09	10.35	11.51	12.11	13.80	2.52	12.19	1.76	5.12	9.70	11.73	4.53	12.63	4.70	10.05
FeO*	18.03	14.45	16.70	17.06	15.71	17.00	15.64	15.70	13.00	15.40	11.59	13.55	16.90	15.76	11.41	17.57	12.93	14.18
MgO	9.51	15.07	9.35	9.08	11.30	10.13	10.96	9.76	14.94	11.12	16.17	14.16	10.62	11.01	15.73	9.89	14.65	11.96
MnO	0.30	0.25	0.37	0.43	0.65	0.65	0.20	0.19	0.23	0.23	0.31	0.36	0.36	0.19	0.19	0.19	0.20	0.20
CaO	10.57	11.57	10.68	10.69	10.50	10.56	10.88	10.93	11.76	10.95	12.08	11.01	10.66	10.96	11.69	10.87	12.08	11.46
Na ₂ O	2.04	0.66	2.09	1.94	1.86	1.96	1.96	2.05	0.72	2.04	0.56	1.15	1.88	1.99	0.83	1.98	0.61	1.35
K ₂ O	0.38	0.13	0.28	0.27	0.22	0.44	0.29	0.35	0.09	0.24	0.07	0.16	0.36	0.29	0.15	0.31	0.15	0.28
F	0.00	0.00	0.00	0.00	0.00	0.00	0.00	0.00	0.00	0.00	0.00	0.00	0.00	0.00	0.00	0.00	0.00	0.00
Cl	0.00	0.00	0.00	0.00	0.00	0.00	0.00	0.00	0.00	0.00	0.00	0.00	0.00	0.00	0.00	0.00	0.00	0.00
Sum	98.37	98.55	97.59	97.26	97.04	97.10	97.46	96.29	97.17	98.09	98.08	97.46	97.27	97.90	97.49	98.30	98.47	97.90
H ₂ O by diff.	1.63	1.45	2.41	2.74	2.96	2.90	2.54	3.71	2.83	1.91	1.92	2.54	2.73	2.10	2.51	1.70	1.53	2.10
Nomenclature	Fe-pargasite	Actinolite	Pargasite	Pargasite	Edenite	Pargasite	Edenite	Pargasite	Actinolite	Edenite	Actinolite	Mg-Hbl	Edenite	Edenite	Mg-Hbl	Edenite	Actinolite	Mg-Hbl
T-sites																		
Si	6.32	7.66	6.38	6.40	6.76	6.58	6.59	6.42	7.77	6.61	7.88	7.46	6.85	6.65	7.54	6.51	7.55	6.95
Aliv	1.68	0.34	1.62	1.60	1.24	1.42	1.41	1.58	0.23	1.39	0.12	0.54	1.15	1.35	0.46	1.49	0.45	1.05
Al(total)	2.41	0.46	2.49	2.46	1.79	2.01	2.09	2.42	0.43	2.09	0.29	0.87	1.69	2.02	0.76	2.18	0.79	1.71
M1,2,3 sites																		
Alvi	0.73	0.13	0.87	0.86	0.55	0.59	0.68	0.84	0.20	0.70	0.18	0.33	0.54	0.66	0.31	0.69	0.34	0.66
Ti	0.04	0.01	0.04	0.04	0.04	0.05	0.04	0.05	0.01	0.04	0.01	0.02	0.04	0.04	0.01	0.05	0.01	0.03
Fe ³⁺	0.69	0.21	0.54	0.55	0.60	0.59	0.53	0.45	0.12	0.50	0.04	0.28	0.48	0.49	0.20	0.56	0.13	0.35
Mg	2.08	3.21	2.05	2.00	2.47	2.24	2.39	2.17	3.21	2.41	3.42	3.04	2.34	2.39	3.35	2.16	3.11	2.57
Mn	0.04	0.03	0.05	0.05	0.08	0.08	0.02	0.02	0.03	0.03	0.04	0.04	0.04	0.02	0.02	0.02	0.02	0.02
Fe ²⁺	1.42	1.41	1.45	1.50	1.26	1.45	1.34	1.48	1.43	1.33	1.31	1.29	1.56	1.39	1.11	1.52	1.38	1.36
Ca	0.00	0.00	0.00	0.00	0.00	0.00	0.00	0.00	0.00	0.00	0.00	0.00	0.00	0.00	0.00	0.00	0.00	0.00
Sum M123	5.00	5.00	5.00	5.00	5.00	5.00	5.00	5.00	5.00	5.00	5.00	5.00	5.00	5.00	5.00	5.00	5.00	5.00
M4 site																		
Fe	0.10	0.11	0.06	0.06	0.07	0.07	0.05	0.03	0.02	0.04	0.02	0.07	0.04	0.04	0.05	0.06	0.03	0.00
Ca	1.66	1.77	1.68	1.69	1.65	1.68	1.71	1.74	1.82	1.70	1.84	1.70	1.69	1.71	1.79	1.70	1.84	1.77
Na	0.24	0.12	0.26	0.25	0.28	0.25	0.24	0.23	0.16	0.25	0.14	0.23	0.28	0.25	0.16	0.23	0.13	0.23
Sum M4	2.00	2.00	2.00	2.00	2.00	2.00	2.00	2.00	2.00	2.00	2.00	2.00	2.00	2.00	2.00	2.00	2.00	2.00
A site																		
Ca	0.00	0.00	0.00	0.00	0.00	0.00	0.00	0.00	0.00	0.00	0.00	0.00	0.00	0.00	0.00	0.00	0.00	0.00
Na	0.34	0.07	0.33	0.31	0.25	0.31	0.31	0.36	0.04	0.32	0.01	0.09	0.26	0.31	0.07	0.33	0.04	0.15
K	0.07	0.02	0.05	0.05	0.04	0.08	0.05	0.07	0.02	0.04	0.01	0.03	0.07	0.05	0.03	0.06	0.03	0.05
Sum A	0.41	0.09	0.39	0.36	0.29	0.39	0.36	0.43	0.06	0.36	0.03	0.12	0.33	0.37	0.09	0.39	0.07	0.20
Sum cations	15.41	15.09	15.39	15.36	15.29	15.39	15.36	15.43	15.06	15.36	15.03	15.12	15.33	15.37	15.09	15.39	15.07	15.20
Fe#	0.52	0.35	0.50	0.51	0.44	0.48	0.44	0.47	0.33	0.44	0.29	0.35	0.47	0.45	0.29	0.50	0.33	0.40
Mg/Fe ²⁺	1.37	2.11	1.36	1.29	1.86	1.47	1.72	1.44	2.21	1.75	2.57	2.24	1.46	1.67	2.88	1.36	2.21	1.89
Mg/Fe	0.94	1.86	1.00	0.95	1.28	1.06	1.25	1.11	2.05	1.29	2.49	1.86	1.12	1.24	2.46	1.00	2.02	1.50

Table C1: Averages of amphibole chemistry from analyzed samples. Textural context (e.g. cores, mantles, rims) and the number of measurements per sample is reported. Nomenclature of amphiboles follows Leake et al. (1997).

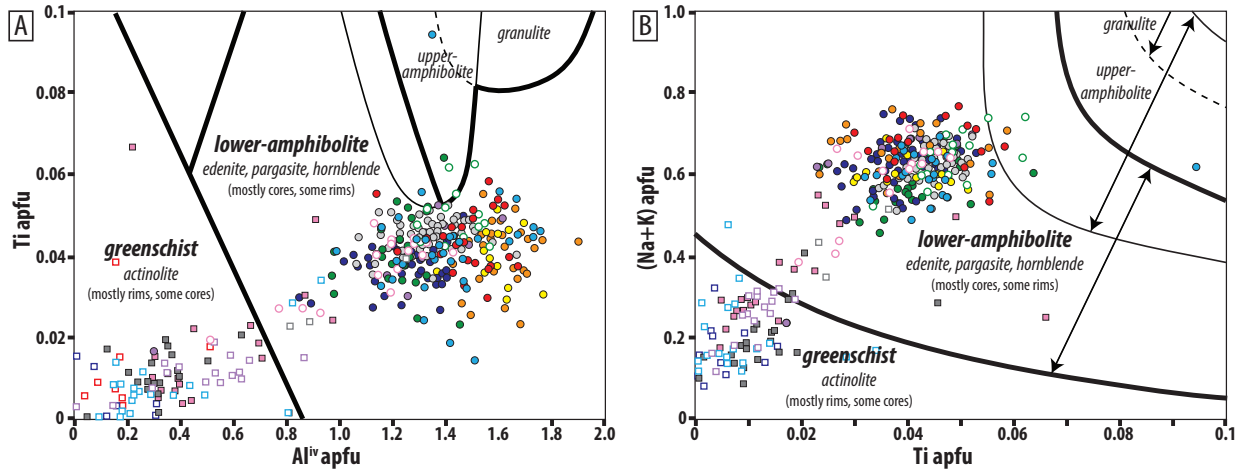


Figure C2: Amphibole point analyses record at least three distinct phases of deformation and metamorphism: prograde D1 greenschist facies, prograde-to-peak D2 lower-amphibolite (epidote-amphibolite) facies, and retrograde D3 greenschist facies. Metamorphic facies fields are from Jin1991. Color key is the same as Figure 6. (A) Al^{iv} vs. Ti atoms p.f.u., and (B) Ti atoms p.f.u. vs. (Na+K) atoms p.f.u. Greenschist facies amphiboles are actinolite, and lower-amphibolite facies amphiboles are edenite, pargasite, and hornblende.

Acknowledgments

This work was funded by a National Science Foundation Graduate Research Fellowship awarded to A.J. Kotowski, the Getty Oil Centennial Professorship to M. Cloos, the UTChron Laboratory at The University of Texas at Austin, and the Chevron (Gulf) Centennial Professorship to D.F. Stockli. Drilling and research in the Oman Drilling Project were supported by the Alfred P. Sloan Foundation (in association with the Deep Carbon Observatory, DCO), the International Continental scientific Drilling Program (ICDP), US National Science Foundation (NSF) Research Grant NSF-EAR-1516300, the Japanese Marine Science and Technology Center (JAMSTEC), the Japanese Society for the Promotion of Science (JSPS), the US National Aeronautics and Space Administration (NASA), the European Science Foundation, the German Science Foundation, the Swiss Science Foundation, and the International Ocean Discovery Program (A.K.A. International Ocean Drilling Program, IODP).

This project was part of A.K.'s Ph.D. dissertation and benefited from many discussions with Whitney Behr and Jaime Barnes. Many thanks to the Structure Team on-board Chikyu: Janos Urai, Michael Kettermann, Yumiko Harigane, Luke Deamer, and Chris MacLeod; to Peter Kelemen, Craig Manning, Juan Carlos de Obeso, and Manuel Menzel for stimulating discussions on topics related to this research; to James Maner for help with XRD and microprobe analyses; and to Lisa Stockli for assistance analyzing and reducing titanite U-Pb data. We are grateful to XX and YY reviewers. Core sample IGSNs are in the SESAR database (<https://www.geosamples.org/>). Bulk geochemistry and electron microprobe data in this manuscript are available on the EarthChem repository (<https://doi.org/10.26022/IEDA/111813>), and titanite U-Pb geochronology is available on Geochron (<https://www.geochron.org/>).

References

- Abbey, S. (1983). Studies in "standard samples" of silicate rocks and minerals 1969-1982. *Can. Geol. Surv. Paper*, 114, 83–15.
- Agard, P., Jolivet, L., Vrielynck, B., Burov, E., & Monie, P. (2007). Plate acceleration: the obduction trigger? *Earth and Planetary Science Letters*, 258(3-4), 428–441.
- Agard, P., Prigent, C., Soret, M., Dubacq, B., Guillot, S., & Deldicque, D. (2020). Slabification: Mechanisms controlling subduction development and viscous coupling. *Earth-Science Reviews*, 103259.
- Agard, P., Yamato, P., Soret, M., Prigent, C., Guillot, S., Plunder, A., ... Monié, P. (2016). Plate interface rheological switches during subduction infancy: Control on slab penetration and metamorphic sole formation. *Earth and Planetary Science Letters*, 451, 208–220.
- Agard, P., Zuo, X., Funicello, F., Bellahsen, N., Faccenna, C., & Savva, D. (2014). Obduction: Why, how and where. clues from analog models. *Earth and Planetary Science Letters*, 393, 132–145.
- Alabaster, T., Pearce, J., & Malpas, J. (1982). The volcanic stratigraphy and petrogenesis of the Oman ophiolite complex. *Contributions to Mineralogy and Petrology*, 81(3), 168–183.
- Aleinikoff, J. N., Wintsch, R. P., Fanning, C. M., & Dorais, M. J. (2002). U–pb geochronology of zircon and polygenetic titanite from the glastonbury complex, connecticut, usa: an integrated sem, empa, tims, and shrimp study. *Chemical Geology*, 188(1-2), 125–147.
- Allemann, F. (1972). The ophiolite radiolarite belt of the North Oman mountains. *Eclogae Geologicae Helveticae*, 65, 657–697.
- Androvičová, A., Čížková, H., & van den Berg, A. (2013). The effects of rheological decoupling on slab deformation in the earth's upper mantle. *Studia Geophysica et Geodaetica*, 57(3), 460–481.
- Apted, M. J., & Liou, J. (1983). Phase relations among greenschist, epidote-amphibolite, and amphibolite in a basaltic system. *American Journal of Science*, 283(A), 328–354.
- Beinlich, A., Plümper, O., Boter, E., Müller, I. A., Kourim, F., Ziegler, M., ... Team, O. D. P. S. (2020). Ultramafic rock carbonation: Constraints from listvenite core bt1b, oman drilling project. *Journal of Geophysical Research: Solid Earth*, 125(6), e2019JB019060.

- Blundy, J., & Holland, T. (1990). Calcic amphibole equilibria and a new amphibole-plagioclase geothermometer. *Contributions to mineralogy and petrology*, 104(2), 208–224.
- Bonamici, C. E., Fanning, C. M., Kozdon, R., Fournelle, J. H., & Valley, J. W. (2015). Combined oxygen-isotope and u-pb zoning studies of titanite: New criteria for age preservation. *Chemical Geology*, 398, 70–84.
- Boudier, F., Bouchez, J., Nicolas, A., Cannat, M., Ceuleneer, G., Misseri, M., & Montigny, R. (1985). Kinematics of oceanic thrusting in the Oman ophiolite: model of plate convergence. *Earth and Planetary Science Letters*, 75(2-3), 215–222.
- Bucher, M. (1991). Mineral equilibria in metagabbros: evidence for polymetamorphic evolution of the Asimah Window, northern Oman Mountains, United Arab Emirates. In *Ophiolite genesis and evolution of the oceanic lithosphere* (pp. 543–571). Springer.
- Çelik, Ö. F., Marzoli, A., Marschik, R., Chiaradia, M., Neubauer, F., & Öz, İ. (2011). Early-middle Jurassic intra-oceanic subduction in the Izmir-Ankara-Erzincan Ocean, northern Turkey. *Tectonophysics*, 509(1-2), 120–134.
- Cherniak, D. (1993). Lead diffusion in titanite and preliminary results on the effects of radiation damage on pb transport. *Chemical Geology*, 110(1-3), 177–194.
- Čížková, H., & Bina, C. R. (2013). Effects of mantle and subduction-interface rheologies on slab stagnation and trench rollback. *Earth and Planetary Science Letters*, 379, 95–103.
- Cloos, M. (1985, jan). Thermal evolution of convergent plate margins: thermal modeling and reevaluation of isotopic Ar-ages for blueschists in the Franciscan Complex of California. *Tectonics*. Retrieved from <http://www.agu.org/pubs/crossref/1985/TC004i005p00421.shtml>papers3://publication/uuid/E3DAF1CA-62E1-464E-B153-D7DA16C13CDD
- Cloos, M., & Shreve, R. L. (1988a). Subduction-channel model of prism accretion, melange formation, sediment subduction, and subduction erosion at convergent plate margins: 1. Background and description. *Pure and Applied Geophysics PAGEOPH*, 128(3-4), 455–500. doi: 10.1007/BF00874548
- Cloos, M., & Shreve, R. L. (1988b, jan). Subduction-channel model of prism accretion, melange formation, sediment subduction, and subduction erosion at convergent plate margins: 1. Background and description. *Pure and Applied Geophysics*, 128(3), 455–500. Retrieved from <http://www.springerlink.com/index/K5K17202P680W850>

- 1017 .pdfpapers3://publication/uuid/C4BF77FD-B4A0-4304-B202-6B3650E5FAC9
- 1018 Coltice, N., G  rault, M., & Ulvrov  , M. (2017). A mantle convection perspective on global
1019 tectonics. *Earth-science reviews*, 165, 120–150.
- 1020 Connelly, J. (2006). Improved dissolution and chemical separation methods for lu-hf garnet
1021 chronometry. *Geochemistry, Geophysics, Geosystems*, 7(4).
- 1022 Cowan, R., Searle, M., & Waters, D. (2014). Structure of the metamorphic sole to the Oman
1023 Ophiolite, Sumeini Window and Wadi Tayyin: implications for ophiolite obduction
1024 processes. *Geological Society, London, Special Publications*, 392(1), 155–175.
- 1025 de Obeso, J. C., Cai, Y., & Kelemen, P. (2018). Strontium isotope profile of Oman Drilling
1026 Project hole BT1B. In *Agu fall meeting abstracts*.
- 1027 Dewey, J. (1976). Ophiolite obduction. *Tectonophysics*, 31(1-2), 93–120.
- 1028 Dewey, J., & Casey, J. (2013). The sole of an ophiolite: the Ordovician Bay of Islands
1029 Complex, Newfoundland. *Journal of the Geological Society*, 170(5), 715–722.
- 1030 Dilek, Y., & Whitney, D. L. (1997). Counterclockwise PTt trajectory from the metamorphic
1031 sole of a Neo-Tethyan ophiolite (Turkey). *Tectonophysics*, 280(3-4), 295–310.
- 1032 Duretz, T., Agard, P., Yamato, P., Ducassou, C., Burov, E. B., & Gerya, T. V. (2016).
1033 Thermo-mechanical modeling of the obduction process based on the Oman ophiolite
1034 case. *Gondwana Research*, 32, 1–10.
- 1035 Ernst, W. (1988). Tectonic history of subduction zones inferred from retrograde blueschist
1036 PT paths. *Geology*, 16(12), 1081–1084.
- 1037 Ernst, W., & Liu, J. (1998). Experimental phase-equilibrium study of Al-and Ti-contents
1038 of calcic amphibole in MORB—a semiquantitative thermobarometer. *American min-
1039 eralogist*, 83(9-10), 952–969.
- 1040 Falk, E. S., & Kelemen, P. B. (2015). Geochemistry and petrology of listvenite in the Samail
1041 ophiolite, Sultanate of Oman: Complete carbonation of peridotite during ophiolite
1042 emplacement. *Geochimica et Cosmochimica Acta*, 160, 70–90.
- 1043 Frost, B. R., Chamberlain, K. R., & Schumacher, J. C. (2001). Sphene (titanite): phase
1044 relations and role as a geochronometer. *Chemical geology*, 172(1-2), 131–148.
- 1045 Garber, J. M., Hacker, B. R., Kylander-Clark, A. R., Stearns, M. A., & E Seward, G. G.
1046 (2017). Assessing the extent of metamorphic transformation in a subducted continental
1047 slab: Titanite petrochronology of the western gneiss region, norway. *EGUGA*, 469.
- 1048 Getsinger, A., & Hirth, G. (2014). Amphibole fabric formation during diffusion creep and
1049 the rheology of shear zones. *Geology*, 42(6), 535–538.

- 1050 Getsinger, A., Hirth, G., Stünitz, H., & Goergen, E. (2013). Influence of water on rheol-
 1051 ogy and strain localization in the lower continental crust. *Geochemistry, Geophysics,*
 1052 *Geosystems*, 14(7), 2247–2264.
- 1053 Ghent, E. D., & Stout, M. Z. (1981, jan). Geobarometry and geothermometry of plagioclase-
 1054 biotite-garnet-muscovite assemblages. *Contributions to Mineralogy and Petrology*,
 1055 76(1), 92–97. Retrieved from [papers3://publication/uuid/E767DA7A-9980-4678-8AE5-973BBFEE28EE](https://pubs.geoscienceworld.org/doi/10.1007/bf01160100)
- 1057 Glennie, K. W. (1974). The geology of the Oman Mountains. *Konin, Nederlands Geol.*
 1058 *Mijnbouw. Genoot. Verdh.*, 31, 423p.
- 1059 Gnos, E. (1998). Peak metamorphic conditions of garnet amphibolites beneath the Se-
 1060 mail ophiolite: implications for an inverted pressure gradient. *International Geology*
 1061 *Review*, 40(4), 281–304.
- 1062 Gnos, E., & Peters, T. (1992). K-Ar ages of the metamorphic sole of the Semail Ophiolite:
 1063 implications for ophiolite cooling history. *Contributions to Mineralogy and Petrology*,
 1064 113(3), 325–332.
- 1065 Godard, M., Bosch, D., & Einaudi, F. (2006). A MORB source for low-Ti magmatism in
 1066 the Semail ophiolite. *Chemical Geology*, 234(1-2), 58–78.
- 1067 Govindaraju, K. (1994). 1994 compilation of working values and sample description for 383
 1068 geostandards. *Geostandards newsletter*, 18, 1–158.
- 1069 Gregory, R. (1984). Melt percolation beneath a spreading ridge: evidence from the semail
 1070 peridotite, oman. *Geological Society, London, Special Publications*, 13(1), 55–62.
- 1071 Guilmette, C., Smit, M. A., van Hinsbergen, D. J., Gürer, D., Corfu, F., Charette, B., ...
 1072 Savard, D. (2018). Forced subduction initiation recorded in the sole and crust of the
 1073 semail ophiolite of oman. *Nature Geoscience*, 11(9), 688–695.
- 1074 Gurnis, M., Hall, C., & Lavier, L. (2004). Evolving force balance during incipient subduction.
 1075 *Geochemistry, Geophysics, Geosystems*, 5(7).
- 1076 Hacker, B. R. (1991, jan). The role of deformation in the formation of metamor-
 1077 phic gradients: Ridge subduction beneath the Oman Ophiolite. *Tectonics*, 10(2),
 1078 455–473. Retrieved from [papers3://publication/uuid/3CE0DA34-DFF4-47D5-91FB-84B25AC9706A](https://pubs.geoscienceworld.org/doi/10.1002/tect.1340100203)
- 1079
- 1080 Hacker, B. R. (1994). Rapid emplacement of young oceanic lithosphere: Argon geochronol-
 1081 ogy of the Oman ophiolite. *Science*, 265(5178), 1563–1565.
- 1082 Hacker, B. R., & Gnos, E. (1997). The conundrum of Samail: explaining the metamorphic

- 1083 history. *Tectonophysics*, 279(1-4), 215–226.
- 1084 Hacker, B. R., & Mosenfelder, J. (1996). Metamorphism and deformation along the em-
 1085 placement thrust of the Samail ophiolite, Oman. *Earth and Planetary Science Letters*,
 1086 144(3-4), 435–451.
- 1087 Hacker, B. R., Mosenfelder, J., & Gnos, E. (1996). Rapid emplacement of the Oman
 1088 ophiolite: Thermal and geochronologic constraints. *Tectonics*, 15(6), 1230–1247.
- 1089 Hawthorne, F. C., Oberti, R., Harlow, G. E., Maresch, W. V., Martin, R. F., Schumacher,
 1090 J. C., & Welch, M. D. (2012). Nomenclature of the amphibole supergroup. *American*
 1091 *Mineralogist*, 97(11-12), 2031–2048.
- 1092 Holland, T., & Blundy, J. (1994). Non-ideal interactions in calcic amphiboles and their bear-
 1093 ing on amphibole-plagioclase thermometry. *Contributions to mineralogy and petrology*,
 1094 116(4), 433–447.
- 1095 Holland, T., & Richardson, S. (1979). Amphibole zonation in metabasites as a guide to
 1096 the evolution of metamorphic conditions. *Contributions to Mineralogy and Petrology*,
 1097 70(2), 143–148.
- 1098 Hopson, C., Coleman, R., Gregory, R., Pallister, J., & Bailey, E. (1981). Geologic sec-
 1099 tion through the Samail ophiolite and associated rocks along a Muscat-Ibra transect,
 1100 southeastern Oman Mountains. *Journal of Geophysical Research: Solid Earth*, 86(B4),
 1101 2527–2544.
- 1102 Ishikawa, T., Nagaishi, K., & Umino, S. (2002). Boninitic volcanism in the Oman ophio-
 1103 lite: Implications for thermal condition during transition from spreading ridge to arc.
 1104 *Geology*, 30(10), 899–902.
- 1105 Jamieson, R. A. (1977). The first metamorphic sodic amphibole identified from the New-
 1106 foundland Appalachians—its occurrence, composition and possible tectonic implica-
 1107 tions. *Nature*, 265(5593), 428.
- 1108 Jamieson, R. A. (1981). Metamorphism during ophiolite emplacement the petrology of the
 1109 St. Anthony Complex. *Journal of Petrology*, 22(3), 397–449.
- 1110 Kelemen, P. B., & Manning, C. E. (2015). Reevaluating carbon fluxes in subduction zones,
 1111 what goes down, mostly comes up. *Proceedings of the National Academy of Sciences*,
 1112 112(30), E3997–E4006.
- 1113 Kelemen, P. B., Matter, J., Streit, E. E., Rudge, J. F., Curry, W. B., & Blusztajn, J.
 1114 (2011). Rates and mechanisms of mineral carbonation in peridotite: natural processes
 1115 and recipes for enhanced, in situ CO₂ capture and storage. *Annual Review of Earth*

- 1116 *and Planetary Sciences*, 39, 545–576.
- 1117 Kennedy, A. K., Kamo, S. L., Nasdala, L., & Timms, N. E. (2010). Grenville skarn titanite:
1118 potential reference material for sims u–th–pb analysis. *The Canadian Mineralogist*,
1119 48(6), 1423–1443.
- 1120 Kohn, M. J. (2017). Titanite petrochronology. *Reviews in Mineralogy and Geochemistry*,
1121 83(1), 419–441.
- 1122 Kohn, M. J., & Corrie, S. L. (2011). Preserved zr-temperatures and u–pb ages in high-grade
1123 metamorphic titanite: evidence for a static hot channel in the himalayan orogen. *Earth
1124 and Planetary Science Letters*, 311(1-2), 136–143.
- 1125 Lafay, R., Godard, M., Beinlich, A., Harris, M., Kelemen, P., & Michibayashi, K. (2019).
1126 Mantle rock carbonation atop the Samail ophiolite metamorphic sole (Oman DP Hole
1127 BT1B): The importance of inherited petrography during large scale metasomatism.
1128 In *Egu general assembly 2019*.
- 1129 Laird, J., & Albee, A. L. (1981). Pressure, temperature, and time indicators in mafic
1130 schist; their application to reconstructing the polymetamorphic history of Vermont.
1131 *American Journal of Science*, 281(2), 127–175.
- 1132 Lallemand, S., Heuret, A., & Boutelier, D. (2005). On the relationships between slab dip,
1133 back-arc stress, upper plate absolute motion, and crustal nature in subduction zones.
1134 *Geochemistry, Geophysics, Geosystems*, 6(9).
- 1135 Leake, B. E., Wooley, A. R., Arps, C. E., Birch, W. D., Gilbert, M. C., Grice, J. D., ...
1136 others (1997). Nomenclature of amphiboles; report of the subcommittee on amphiboles
1137 of the international mineralogical association commission on new minerals and mineral
1138 names. *European Journal of Mineralogy*, 9(3), 623–651.
- 1139 Leng, W., Gurnis, M., & Asimow, P. (2012). From basalts to boninites: The geodynamics of
1140 volcanic expression during induced subduction initiation. *Lithosphere*, 4(6), 511–523.
- 1141 Liou, J., Kuniyoshi, S., & Ito, K. (1974). Experimental studies of the phase relations be-
1142 tween greenschist and amphibolite in a basaltic system. *American Journal of Science*,
1143 274(6), 613–632.
- 1144 Lippard, S. J. (1986). The ophiolite of northern Oman. *Geological Society London Memoir*,
1145 11, 178.
- 1146 Lucassen, F., Dulski, P., Abart, R., Franz, G., Rhede, D., & Romer, R. L. (2010). Re-
1147 distribution of hfse elements during rutile replacement by titanite. *Contributions to
1148 Mineralogy and Petrology*, 160(2), 279–295.

- MacLeod, C. J., Johan Lissenberg, C., & Bibby, L. E. (2013). “Moist MORB” axial magmatism in the Oman ophiolite: The evidence against a mid-ocean ridge origin. *Geology*, *41*(4), 459–462.
- Maruyama, S., Liou, J., & Suzuki, K. (1982). The peristerite gap in low-grade metamorphic rocks. *Contributions to Mineralogy and Petrology*, *81*(4), 268–276.
- Maruyama, S., Suzuki, K., & Liou, J. (1983). Greenschist–amphibolite transition equilibria at low pressures. *Journal of Petrology*, *24*(4), 583–604.
- Massonne, H., & Schreyer, W. (1987). Phengite geobarometry based on the limiting assemblage with K-feldspar, phlogopite, and quartz. *Contributions to Mineralogy and Petrology*, *96*(2), 212–224.
- Massonne, H., & Szpurka, Z. (1997, jan). Thermodynamic properties of white micas on the basis of high-pressure experiments in the systems $\text{K}_2\text{O} - \text{MgO} - \text{Al}_2\text{O}_3 - \text{SiO}_2 - \text{H}_2\text{O}$ and $\text{K}_2\text{O} - \text{FeO} - \text{Al}_2\text{O}_3 - \text{SiO}_2 - \text{H}_2\text{O}$. *Lithos*. Retrieved from <http://linkinghub.elsevier.com/retrieve/pii/S0024493797820142papers3://publication/uuid/AEFBC8EE-F5DA-4307-800B-0C75493EFE5F>
- Menzel, M. D., Urai, J., de Obeso, J. C., Kotowski, A., Manning, C. E., Kelemen, P. B., ... Harigane, Y. (2020). Brittle deformation of carbonated peridotite—insights from listvenites of the samail ophiolite (oman drilling project hole bt1b).
- Mezger, K., Rawnsley, C., Bohlen, S., & Hanson, G. (1991). U–pb garnet, sphene, monazite, and rutile ages: implications for the duration of high-grade metamorphism and cooling histories, adirondack mts., new york. *The Journal of Geology*, *99*(3), 415–428.
- Nicolas, A., Reuber, I., & Benn, K. (1988). A new magma chamber model based on structural studies in the Oman ophiolite. *Tectonophysics*, *151*(1–4), 87–105.
- Odlum, M., & Stockli, D. (2019). Thermotectonic evolution of the north pyrenean agly massif during early cretaceous hyperextension using multi-mineral u–pb thermochronometry. *Tectonics*, *38*(5), 1509–1531.
- Paton, C., Woodhead, J. D., Hellstrom, J. C., Hergt, J. M., Greig, A., & Maas, R. (2010). Improved laser ablation u–pb zircon geochronology through robust downhole fractionation correction. *Geochemistry, Geophysics, Geosystems*, *11*(3).
- Pearce, J. A., Alabaster, T., Shelton, A., & Searle, M. P. (1981). The Oman ophiolite as a Cretaceous arc-basin complex: evidence and implications. *Philosophical Transactions of the Royal Society of London. Series A, Mathematical and Physical Sciences*, *300*(1454), 299–317.

- 1182 Pearce, J. A., & Norry, M. J. (1979). Petrogenetic implications of Ti, Zr, Y, and Nb
1183 variations in volcanic rocks. *Contributions to mineralogy and petrology*, 69(1), 33–47.
- 1184 Petrus, J. A., & Kamber, B. S. (2012). Vizualage: A novel approach to laser ablation icp-ms
1185 u-pb geochronology data reduction. *Geostandards and Geoanalytical Research*, 36(3),
1186 247–270.
- 1187 Platt, J. P. (1975, jan). Metamorphic and deformational processes in the Fran-
1188 ciscan Complex, California; some insights from the Catalina Schist ter-
1189 rane. *Geological Society of America Bulletin*, 86(10), 1337–1347. Retrieved
1190 from [http://www.ncbi.nlm.nih.gov/entrez/query.fcgi?db=pubmed{\&}cmd=](http://www.ncbi.nlm.nih.gov/entrez/query.fcgi?db=pubmed{\&}cmd=Retrieve{\&}dopt=AbstractPlus{\&}list{_}uids=71683709056587705related:uReAHvSr{_}gAJpapers3://publication/uuid/FDCC037A-7228-4048-A5E0-7F4C30087C5A)
1191 [Retrieve{\&}dopt=AbstractPlus{\&}list{_}uids=71683709056587705related:](http://www.ncbi.nlm.nih.gov/entrez/query.fcgi?db=pubmed{\&}cmd=Retrieve{\&}dopt=AbstractPlus{\&}list{_}uids=71683709056587705related:uReAHvSr{_}gAJpapers3://publication/uuid/FDCC037A-7228-4048-A5E0-7F4C30087C5A)
1192 [uReAHvSr{_}gAJpapers3://publication/uuid/FDCC037A-7228-4048-A5E0](http://www.ncbi.nlm.nih.gov/entrez/query.fcgi?db=pubmed{\&}cmd=Retrieve{\&}dopt=AbstractPlus{\&}list{_}uids=71683709056587705related:uReAHvSr{_}gAJpapers3://publication/uuid/FDCC037A-7228-4048-A5E0-7F4C30087C5A)
1193 [-7F4C30087C5A](http://www.ncbi.nlm.nih.gov/entrez/query.fcgi?db=pubmed{\&}cmd=Retrieve{\&}dopt=AbstractPlus{\&}list{_}uids=71683709056587705related:uReAHvSr{_}gAJpapers3://publication/uuid/FDCC037A-7228-4048-A5E0-7F4C30087C5A)
- 1194 Plunder, A., Agard, P., Chopin, C., Soret, M., Okay, A. I., & Whitechurch, H. (2016). Meta-
1195 morphic sole formation, emplacement and blueschist facies overprint: early subduction
1196 dynamics witnessed by western Turkey ophiolites. *Terra Nova*, 28(5), 329–339.
- 1197 Poli, S., & Schmidt, M. W. (1995). H₂O transport and release in subduction zones: experi-
1198 mental constraints on basaltic and andesitic systems. *Journal of Geophysical Research:*
1199 *Solid Earth*, 100(B11), 22299–22314.
- 1200 Raase, P. (1974). Al and Ti contents of hornblende, indicators of pressure and temperature of
1201 regional metamorphism. *Contributions to mineralogy and petrology*, 45(3), 231–236.
- 1202 Reichen, L. E., Fahey, J. J., et al. (1962). Improved method for the determination of FeO
1203 in rocks and minerals including garnet.
- 1204 Rioux, M., Bowring, S., Kelemen, P., Gordon, S., Dudás, F., & Miller, R. (2012). Rapid
1205 crustal accretion and magma assimilation in the Oman-UAE ophiolite: High precision
1206 U-Pb zircon geochronology of the gabbroic crust. *Journal of Geophysical Research:*
1207 *Solid Earth*, 117(B7).
- 1208 Rioux, M., Bowring, S., Kelemen, P., Gordon, S., Miller, R., & Dudás, F. (2013). Tectonic
1209 development of the Samail ophiolite: High-precision U-Pb zircon geochronology and
1210 Sm-Nd isotopic constraints on crustal growth and emplacement. *Journal of Geophys-*
1211 *ical Research: Solid Earth*, 118(5), 2085–2101.
- 1212 Rioux, M., Garber, J., Bauer, A., Bowring, S., Searle, M., Kelemen, P., & Hacker, B. R.
1213 (2016). Synchronous formation of the metamorphic sole and igneous crust of the Semail
1214 ophiolite: New constraints on the tectonic evolution during ophiolite formation from

- high-precision U–Pb zircon geochronology. *Earth and Planetary Science Letters*, 451, 185–195.
- Roberts, N. M., Thomas, R. J., & Jacobs, J. (2016). Geochronological constraints on the metamorphic sole of the semail ophiolite in the united arab emirates. *Geoscience Frontiers*, 7(4), 609–619.
- Ruh, J. B., Le Pourhiet, L., Agard, P., Burov, E., & Gerya, T. (2015). Tectonic slicing of subducting oceanic crust along plate interfaces: Numerical modeling. *Geochemistry, Geophysics, Geosystems*, 16(10), 3505–3531.
- Searle, M. P., & Cox, J. (1999). Tectonic setting, origin, and obduction of the Oman ophiolite. *Geological Society of America Bulletin*, 111(1), 104–122.
- Searle, M. P., & Cox, J. (2002). Subduction zone metamorphism during formation and emplacement of the semail ophiolite in the oman mountains. *Geological Magazine*, 139(3), 241–255.
- Searle, M. P., & Malpas, J. (1980). Structure and metamorphism of rocks beneath the Semail ophiolite of Oman and their significance in ophiolite obduction. *Earth and Environmental Science Transactions of the Royal Society of Edinburgh*, 71(4), 247–262.
- Searle, M. P., & Malpas, J. (1982). Petrochemistry and origin of sub-ophiolitic metamorphic and related rocks in the Oman Mountains. *Journal of the Geological Society*, 139(3), 235–248.
- Searle, M. P., Waters, D., Garber, J., Rioux, M., Cherry, A., & Ambrose, T. (2015). Structure and metamorphism beneath the obducting Oman ophiolite: Evidence from the Bani Hamid granulites, northern Oman mountains. *Geosphere*, 11(6), 1812–1836.
- Searle, M. P., Waters, D., Martin, H., & Rex, D. (1994). Structure and metamorphism of blueschist–eclogite facies rocks from the northeastern Oman Mountains. *Journal of the Geological Society*, 151(3), 555–576.
- Shervais, J. W. (1982). Ti–V plots and the petrogenesis of modern and ophiolitic lavas. *Earth and planetary science letters*, 59(1), 101–118.
- Shido, F., & Miyashiro, A. (1959). Hornblendes of basic metamorphic rocks. *J. Fac. Sci. Univ. Tokyo*, 2, 12–102.
- Soret, M., Agard, P., Dubacq, B., Plunder, A., & Yamato, P. (2017). Petrological evidence for stepwise accretion of metamorphic soles during subduction infancy (Semail ophiolite, Oman and UAE). *Journal of Metamorphic Geology*, 35(9), 1051–1080.

- 1248 Soret, M., Agard, P., Ildefonse, B., Dubacq, B., Prigent, C., & Rosenberg, C. (2019).
 1249 Deformation mechanisms in mafic amphibolites and granulites: record from the semail
 1250 metamorphic sole during subduction infancy. *Solid Earth*, 10(5), 1733–1755.
- 1251 Spear, F. S. (1995). Metamorphic phase equilibria and pressure-temperature-time paths.
- 1252 Spencer, K., Hacker, B., Kylander-Clark, A., Andersen, T., Cottle, J., Stearns, M., ...
 1253 Seward, G. (2013). Campaign-style titanite u–pb dating by laser-ablation icp: Impli-
 1254 cations for crustal flow, phase transformations and titanite closure. *Chemical Geology*,
 1255 341, 84–101.
- 1256 Stacey, J., & Kramers, J. (1975). Approximation of terrestrial lead isotope evolution by a
 1257 two-stage model. *Earth and Planetary Science Letters*, 26(2), 207–221.
- 1258 Stern, R. J., & Bloomer, S. H. (1992). Subduction zone infancy: examples from the
 1259 Eocene Izu-Bonin-Mariana and Jurassic California arcs. *Geological Society of America*
 1260 *Bulletin*, 104(12), 1621–1636.
- 1261 Stern, R. J., Reagan, M., Ishizuka, O., Ohara, Y., & Whattam, S. (2012). To under-
 1262 stand subduction initiation, study forearc crust: To understand forearc crust, study
 1263 ophiolites. *Lithosphere*, 4(6), 469–483.
- 1264 Styles, M., Ellison, R., Arkley, S., Crowley, Q. G., Farrant, A., Goodenough, K. M., ...
 1265 others (2006). The geology and geophysics of the united arab emirates: Volume 2,
 1266 geology.
- 1267 Tilton, G., Hopson, C., & Wright, J. (1981). Uranium-lead isotopic ages of the Samail ophio-
 1268 lite, Oman, with applications to Tethyan ocean ridge tectonics. *Journal of Geophysical*
 1269 *Research: Solid Earth*, 86(B4), 2763–2775.
- 1270 van Keken, P. E., Hacker, B. R., Syracuse, E. M., & Abers, G. A. (2011). Subduction
 1271 factory: 4. Depth-dependent flux of H₂O from subducting slabs worldwide. *Journal*
 1272 *of Geophysical Research*, 116, B01401, doi:10.1029/2010JB007922.
- 1273 Velde, B. (1965). Phengite micas; synthesis, stability, and natural occurrence. *American*
 1274 *Journal of Science*, 263(10), 886–913.
- 1275 Vermeesch, P. (2018). Isoplotr: A free and open toolbox for geochronology. *Geoscience*
 1276 *Frontiers*, 9(5), 1479–1493.
- 1277 Wada, I., & Wang, K. (2009). Common depth of slab-mantle decoupling: Reconciling
 1278 diversity and uniformity of subduction zones. *Geochemistry, Geophysics, Geosystems*,
 1279 10(10).
- 1280 Wada, I., Wang, K., He, J., & Hyndman, R. D. (2008). Weakening of the subduction

- 1281 interface and its effects on surface heat flow, slab dehydration, and mantle wedge
 1282 serpentinization. *Journal of Geophysical Research: Solid Earth*, 113(B4).
- 1283 Wakabayashi, J., & Dilek, Y. (2000). Spatial and temporal relationships between ophiolites
 1284 and their metamorphic soles: a test of models of forearc ophiolite genesis. *SPECIAL
 1285 PAPERS-GEOLOGICAL SOCIETY OF AMERICA*, 53–64.
- 1286 Warren, C. J., Parrish, R. R., Searle, M. P., & Waters, D. J. (2003). Dating the subduction
 1287 of the Arabian continental margin beneath the Semail ophiolite, Oman. *Geology*,
 1288 31(10), 889–892.
- 1289 Warren, C. J., Parrish, R. R., Waters, D. J., & Searle, M. P. (2005). Dating the geologic
 1290 history of oman’s semail ophiolite: Insights from u-pb geochronology. *Contributions
 1291 to Mineralogy and Petrology*, 150(4), 403–422.
- 1292 Wendt, A. S., D’Arco, P., Goffé, B., & Oberhänsli, R. (1993). Radial cracks around α -
 1293 quartz inclusions in almandine: constraints on the metamorphic history of the Oman
 1294 Mountains. *Earth and Planetary Science Letters*, 114(4), 449–461.
- 1295 Whattam, S. A., & Stern, R. J. (2011). The ‘subduction initiation rule’: a key for linking
 1296 ophiolites, intra-oceanic forearcs, and subduction initiation. *Contributions to Miner-
 1297 alogy and Petrology*, 162(5), 1031–1045.
- 1298 Williams, H., & Smyth, W. (1973). Metamorphic aureoles beneath ophiolite suites and
 1299 alpine peridotites; tectonic implications with west Newfoundland examples. *American
 1300 Journal of Science*, 273(7), 594–621.
- 1301 Yakymchuk, C., Clark, C., & White, R. W. (2017). Phase relations, reaction sequences and
 1302 petrochronology. *Reviews in Mineralogy and Geochemistry*, 83(1), 13–53.